DR JEAN JOSEPH HOOGHVORST (Orcid ID : 0000-0001-5975-6169)

DR MARIA A. NIKOLINAKOU (Orcid ID : 0000-0003-3194-3477)

DR OSCAR FERNANDEZ (Orcid ID : 0000-0003-1584-2684)

PROFESSOR PETER BARRY FLEMINGS (Orcid ID : 0000-0002-5377-3694)

DR ALEJANDRO MARCUELLO (Orcid ID : 0000-0002-6216-4436)

Article type : Research Article

Geologically constrained evolutionary geomechanical modelling of diapir and basin evolution: A case study from the Tarfaya basin, West African coast

Jean Joseph Hooghvorst (Corresponding author)

Dept. Dinàmica de la Terra i de l'Oceà, Facultat de Ciencies de la Terra, Universitat de Barcelona, Martí I Franqués, s/n, 08028 Barcelona, Spain; jeanjo_90@hotmail.com

Maria A. Nikolinakou

Bureau of Economic Geology, Jackson School of Geosciences, The University of Texas at Austin, 10100 Burnet Road, Building PRC-130, Austin, TX 78758, USA; mariakat@mail.utexas.edu

Toby W. D. Harrold

P-TEN Geomechanics Services S.L., Camino Nuevo 203, Alcobendas, 28109, Madrid, Spain;

toby.harrold@p-ten.com

Oscar Fernandez

Dept. Geodynamics and Sedimentology, University of Vienna, Althanstrasse 14, 1090, Vienna, Austria; esparita@gmail.com

Peter B. Flemings

Dept. of Geological Sciences and Institute for Geophysics, Jackson School of Geosciences, The University of Texas at Austin, 1 University Station C1100, Austin, TX 78712, USA; Pflemings@jsg.utexas.edu

Alejandro Marcuello

Inst. Geomodels, Dept. Dinàmica de la Terra i de l'Oceà, Facultat de Ciencies de la Terra, Univeristat de Barcelona, Martí I Franqués, s/n, 08028 Barcelona, Spain; alex.marcuello@ub.edu

ABSTRACT

We systematically incorporate burial history, sea floor geometry, and tectonic loads from a sequential kinematic restoration model into a 2D evolutionary geomechanical model that simulates the formation of the Sandia salt diapir, Tarfaya basin, NW African Coast. We use a poro-elastoplastic description for the sediment behaviour and a visco-plastic description for the salt. Sedimentation is coupled with salt flow and regional shortening to determine the sediment porosity and strength and to capture the interaction between salt and sediments. We find that temporal and spatial variation in sedimentation rate is a key control on the kinematic evolution of the salt system. Incorporation of sedimentation rates from the kinematic restoration at a location east of Sandia leads to a final geomechanical model geometry very similar to that observed in seismic reflection data. We also find that changes in the variation of shortening rates can significantly affect the present-day stress state above salt. Overall, incorporating kinematic restoration data into evolutionary models provides insights into the key parameters that control the evolution of geologic systems. Furthermore, it enables more realistic evolutionary geomechanical models, which, in turn, provide insights into sediment stress and porosity.

Keywords: kinematic restoration, burial history, evolutionary geomechanical model, salt tectonics, Sandia diapir, Tarfaya basin

HIGLIGHTS

High sedimentation rates during Jurassic is the key driver for the Sandia diapir evolution

The Atlas shortening reactivates the Tarfaya diapirs during Late Cretaceous by mobilizing salt towards the crest

Higher sedimentation rates at early stages of diapir formation affect whether the diapir will upbuild to the sea floor

Different shortening rates have significant effect on present-day stress state above Sandia

INTRODUCTION

The study of the formation and evolution of sedimentary basins provides valuable information on the key geological processes that led to the present-day geometry and state of stress and pore pressure. Both inverse (kinematic restoration) and forward (physical, basin, and geomechanical modelling) approaches have been developed to identify and study the fundamentals of these processes.

Kinematic restoration (McGuinness & Hossack 1993; Rowan 1993; Hudec & Jackson 2004; Trudgill & Rowan 2004; Rowan *et al.* 2016) is an inverse approach that starts with the present-day geometry of a basin and reconstructs past deformation states by taking into account deposition of sediments and their compaction, eustasy, fault-controlled deformations, isostasy, thermal subsidence and salt movements (Rowan & Ratliff 2012). However, this method does not simulate the evolution of stresses during the basin restoration. In addition, established kinematic restoration techniques of salt systems do not explicitly model salt flow. Recently, there have been efforts to combine kinematic restorations with finite-element modelling (Maerten & Maerten 2006; Moretti & Guiton 2006; Durand-Riard *et al.* 2013; Crook *et al.* 2018). These approaches simulate the stress-strain behaviour of sediments to better approximate the past deformation of the studied systems but do not include viscous laws for the salt flow.

Physical (analogue) modelling is a forward method that studies the evolution of geologic systems using rock analogues with predefined rheologies and boundary conditions within a laboratory setup that deforms at smaller spatial and temporal scales (Schellart & Strak 2016; Reber *et al.* 2020). The rules for model scaling were initially established by King Hubbert (Hubbert 1937) using three aspects of similarity: geometric, kinematic and dynamic (Koyi 1997). Physical models have been used to represent a wide variety of processes including strike-slip fault systems (Hubbert 1951; Dooley & Schreurs 2012; Corti & Dooley 2015), fold and thrust belts (e.g., Ramberg 1981; Massoli *et al.* 2006; Nilforoushan & Koyi 2007; Farzipour-Saein & Koyi 2014), plutonism (Dietl & Koyi 2011) or salt-related deformation (e.g., Koyi 1998; Dooley *et al.* 2015, 2017; Dooley & Hudec 2017). The principal limitations of these models are associated with material and topography scaling, leading to uncertainty on the timing and duration of the geological processes, exaggerated topographies, and no information on the internal stress state of the modelled systems and its evolution through time (Schellart & Strak 2016). Furthermore, model reproducibility is highly related to human factors affecting the model set-up (Schreurs *et al.* 2016). Despite these limitations, physical modelling is a particularly strong tool for investigating and visualizing geologic processes.

Basin modelling is another forward method that studies geological processes in sedimentary basins using geological, petrophysical, geophysical and geochemical data (Hantschel & Kauerauf 2009). Basin modelling has been extensively used by the oil and gas industry to model petroleum systems. Simulated processes range from deposition and compaction, erosion, heat flow, phase dissolution, to hydrocarbon generation and its accumulation and migration (Ben-Awuah *et al.* 2013). Some basin models incorporate stress and/or pressure calculations. However, the method commonly assumes that the sediments deform uniaxially, hence it cannot capture stress, strain and pore pressure perturbations caused by complex deformation processes such as faulting or halokinesis (e.g., Bolas *et al.* 2004; Gutierrez & Wangen 2005, Stigall & Dugan 2010; Thibaut *et al.* 2014).

Recent advances in understanding the evolution of geological systems result from the incorporation of non-uniaxial deformation in basin models and the introduction of poromechanical numerical models (Beaumont *et al.* 2000; Kaus *et al.* 2008; Albertz & Beaumont 2010; Fernandez & Kaus 2015; Nikolinakou *et al.* 2018b). Poromechanical (geomechanical) models, in particular, incorporate coupled porous fluid flow and the full stress tensor in modelling the compression behaviour and strength of sediments. Geomechanical models are now commonly used for the study of hydrocarbon prospects, especially in non-uniaxial frontier settings such as salt systems or compressional systems (e.g., Willson *et al.* 2002; Dusseault *et al.* 2004). Static geomechanical models are often built using the basin geometry at present day (e.g., acquired from seismic data), and can provide a first-order estimate of stress and pressure around existing structures (e.g., Fredrich *et al.* 2007b; Segura *et al.* 2016; Heidari *et al.* 2018a; Hooghvorst *et al.* 2020). Stress calculation, however, lacks input from past geological processes during the evolution of the structures (Nikolinakou *et al.* 2014). Evolutionary geomechanical (forward) modelling, on the other hand, can simulate time-dependent processes, such as deposition, tectonic loading, salt flow, and porous fluid flow. Hence, it couples the deformation and strength of sediments with the development of geologic systems (Goteti *et al.* 2012; Gradmann & Beaumont 2012; Gradmann *et al.* 2012; Nikolinakou *et al.* 2018a; Hamilton-Wright *et al.* 2019; Thigpen *et al.* 2019). The principal limitation of the evolutionary models is the difficulty in producing the observed present-day geometry (Nikolinakou *et al*. 2014). To the best of our knowledge, very few studies have tried to incorporate the geologic history of a given basin into an evolutionary geomechanical model (e.g., Crook *et al.* 2018; Thigpen *et al.* 2019).

Our study is one of the first systematic approaches to incorporate burial history, sea floor geometry, and tectonic loads from a sequential kinematic restoration into an evolutionary geomechanical model of a salt basin. In addition to using the kinematic restoration to constrain the geomechanical model, we employ a poromechanical description of sediment behaviour to capture the interaction between salt movement, sediment deposition, and deformation and to study parameters that drive the salt-system evolution. We simulate the development of the Sandia diapir in the Tarfaya basin, West African Coast, and compare our model predictions with the inferred kinematic evolution of the basin. We find that the depositional history, and especially the variation in early sedimentation rates, is the key parameter that drives the evolution of the Sandia diapir to its present-day geometry. We also illustrate the importance of tectonic shortening to diapirism and the present-day stress state. Overall, we show that careful representation of the depositional and tectonic history can enable more realistic evolutionary geomechanical models, with final model geometries that resemble the seismic interpretation of geologic structures.

GEOLOGICAL CONTEXT

The Tarfaya Basin is a passive continental margin basin located offshore SW Morocco (Gouiza 2011) and bound by the Agadir and Essaouira Basins to the north and by the Aaiun Basin to the south (Figure 1). On the west, the basin ends against the eastern Canary Islands (Lanzarote and Fuerteventura islands) and the Conception Bank, that separate it from the deep abyssal plain. To the east, the basin is bound on the onshore, from north to south, by the Atlas belt, the Anti-Atlas and their undeformed foreland. At present, a SW-NE trending, 2000 m deep bathymetric trough defines the most distal part of the basin at the edge of the continental shelf.

The Tarfaya basin formed during Late Triassic to Early Jurassic rifting and opening of the Central Atlantic and the separation of the NW African margin from the North American margin. Rifting caused extension of the basement, forming fault-controlled half-grabens trending NNE-SSW to NE-SW (Piqué *et al.* 1998; Le Roy & Piqué 2001), which were infilled by thick syn-rift sequences of continental siliciclastic red beds and evaporites of Triassic age. The Triassic evaporites are the source layer for the present-day salt-cored structures in this area (Tari & Jabour 2013).

During the Jurassic, post-breakup thermal subsidence of the basin caused the western part to deepen. A carbonate platform formed along the eastern, shallower, continental margin. Initial development of salt structures began during the Jurassic and continued during Early Cretaceous, affecting the sea floor surface at these times (Michard *et al.* 2008). The location of individual salt structures was strongly controlled by the uneven distribution of Triassic salt thickness within the half-graben system (Tari & Jabour 2013).

A relative sea-level fall during the Late Jurassic–Early Cretaceous (Berriasian to Valanginian) caused subaerial exposure and karstification of the carbonate platform. This was followed by sedimentation of alluvial siliciclastic materials forming the Tan Tan Delta complex (Michard *et al.* 2008; Wenke *et al.* 2011).

The Tarfaya basin was then compressed by inversion of the Atlas and uplift of northwestern Africa. This started during the Late Cretaceous (Coniacian) and lasted until the Quaternary with episodes of activity followed by quiescence (Frizon de Lamotte *et al.* 2008). Atlasic uplift increased the sediment input (Wenke *et al.* 2011) and the compression reactivated pre-existing salt structures formed during the Jurassic and Early Cretaceous (Tari & Jabour 2013). In addition, volcanic emplacement of the Canary Islands archipelago occurred during the Cenozoic (Carracedo & Perez-Torrado 2013).

STRUCTURE AND EVOLUTION

The study area is located at the most distal part of the Tarfaya Basin (Figure 1) and centres around the Sandia and the Western diapirs (Figure 2). Seismic interpretation of proprietary 3D seismic migrated in time and depth was complemented with vintage 2D reflection multi-channel seismic profiles (acquired in 1983) migrated in time. Interpretation was constrained with data from two exploration wells. The Cap Juby-1 well (black triangle, Figure1) was drilled by Mobil in 1983 and reached diapiric Triassic evaporites below Upper Jurassic carbonates. The Sandia-1 well (black circle, Figure 1) was drilled by Repsol in 2015 and reached Paleocene siliciclastics above the Sandia salt diapir (Figure 2).

The good quality of the seismic data in the shallowest 5 km together with the well data make the interpretation of the Tertiary section straightforward (Figure 2). The interpretation of the deeper units is more ambiguous because of the different geologic history of the deeper water basin (in the NW) compared to the shallower platform area (in the SE), where the Cap Juby-1 control well is located. In the platform area, the Jurassic and Triassic units are found at shallower depths as a result of the Atlasic inversion that started in the Late Cretaceous. Seismic reflection data suggests that this Atlasic inversion resulted in significant erosional truncation of units and accounted for 500-1000 m of uplift of the shelf area. Because thicknesses of pre-inversion (Mesozoic) units in the platform area were used as guides for their interpretation in the deep-water sector (Figure 2), there is more uncertainty in the interpretation of deeper units.

The key regional-scale feature of the study area is a thick Tertiary basin (up to 4 km thick) in the deep-water domain (Figure 2). This Tertiary basin wedges towards the SE onto the continental shelf and overlies a regional erosional unconformity in the continental shelf and across the shelf break. Basinward, and barring areas deformed by diapirism, Tertiary units lie conformably over Cretaceous sediments. Both Tertiary and Mesozoic (Jurassic and Cretaceous) sediments display thickness changes and deformation related to diapirism of the underlying Triassic evaporites. These evaporites cut through the overlying units in the form of diapirs at two locations on this cross-section (Figure 2).

Published observations of half-graben geometries suggest that these salt diapirs may have nucleated above rotated basement fault-blocks along the Moroccan Atlantic margin (Le Roy &

Piqué 2001; Tari & Jabour 2013). The basinward diapir (Western diapir) is active at present-day and deforms the seabed. The landward diapir (Sandia diapir), which was the target of the Sandia-1 exploratory well (black circle, Figure 1), ceased growth during the Tertiary. Both diapirs display geometries that are consistent with passive down-building development during the Mesozoic, and a phase of lateral expansion during the Cretaceous. Folding of Paleogene strata above the diapirs indicates that they were reactivated by shortening during the Tertiary. Shortening caused further growth of the Western diapir and extrusion onto the seabed. However, in the case of the Sandia diapir, shortening only caused folding of the overburden and lateral flow of salt toward the centre of the salt structure.

The geomechanical model we present is based on a sequential kinematic restoration of the regional cross-section to Triassic times, during the deposition of the evaporites (Figure 3). This restoration accounted for decompaction of sediments by assuming average shale or sandy shale lithology and compaction curves of Sclater & Christie (1980). Despite the presence of carbonates in the Jurassic section of the shallow-water domain, the restoration assumed sandy-shale materials for the entire Jurassic. This is the expected lithology in the deeper part of the basin, which is the objective of the geomechanical modelling. The restoration also considered local isostasy and corrected for the effect of thermal subsidence by applying the curves of McKenzie (1978) (the beta factor was estimated from the expected crustal thickness based on the interpreted top of the basement and assuming an isostatically equilibrated crust). It accounted for the effects of salt diapirism following the approach of Rowan & Ratliff (2012). Finally, the sequential restoration accounted for the Atlasic shortening of 5 km based on the unfolded length of the Cretaceous – Paleocene horizon, considered to be pre-Atlasic.

EVOLUTIONARY MODEL DEFINITION

We built a series of 2D plane-strain evolutionary geomechanical models using the finite element program Elfen (Rockfield 2017). A base-case model (BC, Table 1) is used as reference model for comparison in a series of sensitivity analyses. A number of model variants (MV, Table 1) explore the influence of selected input parameters. Each variant modifies one parameter compared to the BC model (Table 1).

Base-case model (BC)

The base-case (BC) model has an initial geometry that includes a two-km thick salt layer and a shale layer averaging 1.1 km thickness on top (Figure 4). The role of the shale layer is to preserve the initial geometry of the salt top surface by preventing the salt from moving laterally towards the minibasins during the model (gravity) initialization step. We introduce an initial seed (in the form of a small salt dent circled in Figure 4a) at the centre of the salt top surface and a slight sag of the salt surface at both sides of the seed to facilitate the initiation of the salt diapir. Displacements are constrained in both the horizontal and vertical directions at the base of the model and only in the horizontal direction at the sides of the model.

We use both a burial history curve (Figure 5a) and the paleo-bathymetries provided by the sequential kinematic restoration model (Figure 3) as boundary conditions for the evolutionary model (Figure 4b). To obtain the burial history for the simulation of the Sandia diapir (Figure 5a), we extract the thickness of sedimentary layers from the kinematic restoration model along a vertical location 10 km east of the diapir (location Y; Figure 3), at the end of each geologic interval (Table 2). The shallowest layer at each geologic interval in the restoration model is de-compacted and, hence, its thickness is used in the evolutionary model with no further adjustment: for each modelled geologic interval, the deposited-layer thickness provided by the burial history curve (Figure 5a) is added to the current sea floor in the evolutionary model to define the elevation of the upcoming deposition horizon (Figure 4b). This calculation is applied at the right end of the evolutionary model, 30 km from the Sandia diapir, to ensure far-field conditions (arrow in location A, Figure 4b). We extend the deposition horizon across the model using an average bathymetric slope (Table 2), which we determine from the kinematic restoration by measuring the average sea floor slope angle at each geologic interval. We then simulate deposition in the evolutionary model by filling the space between the current sea floor and the upcoming horizon (Figure 4b).

The movement of the salt in this evolutionary model is not prescribed. The differential loading imposed by the weight of the deposited material causes the salt to deform and flow. This, together with sediment compaction, modifies the topography of the sea floor in the model. Because the seafloor geometry at the end of a given deposition step becomes the baseline for the next deposition stage, the upper surface of each deposition horizon depends on both the burial history and the preceding model evolution (e.g., Early Cretaceous stage, Figure 4b).

We simulate the tectonic shortening between Upper Cretaceous (100 Ma) and the present day by imposing shortening on the model that deforms it from its original length of 65 km to a final length of 60 km. The shortening deformation rate increases gradually over the first 50 Myr to ensure numerical stability and follows an exponential curve thereafter (solid curve, Figure 4c).

The salt is modelled using the Munson-Dawson formulation (Appendix A; Munson & Dawson 1979). The Munson-Dawson model has been extensively used to simulate the viscous flow of salt in deep-water salt basins such as Gulf of Mexico, West African coast, or offshore Brazil (Fredrich *et al.* 2003; Marketos *et al.* 2016; Segura *et al.* 2016; Thigpen *et al.* 2019; Hooghvorst *et al.* 2020). The salt viscosity depends on both differential stress and temperature. Because of the absence of field data, input parameters for the salt (Where $\dot{\varepsilon}_c$ is the salt viscosity, q is the shear stress, T is the temperature, R is the universal gas constant, μ is the shear modulus and A_1, A_2 n_1, n_2 are material constants.

Table 3, in Appendix A) are calibrated based on Avery Island salt (Munson 1997; Fredrich *et al.* 2007a), which is considered to represent average behaviour for Gulf of Mexico salt. The initial salt stress state is uniform (K_0 = 1, see Appendix B for nomenclature), but differential stresses develop later in the model because of sediment loading. In addition, we assume the salt to be a homogeneous and isotropic material and we do not account for inner layering and anisotropies. A temperature gradient of 3.1°C per 100 m is used (e.g., Rimi 2001; Zarhloule *et al.* 2010), starting with a sea floor temperature of 4°C. This gradient is based on an integrated 2D and 3D petroleum system model for thermal maturity evaluation.

The sediment is modelled as a porous elastoplastic material using the SR3 constitutive model (Crook *et al.* 2006, see Appendix A). This model is based on the critical state theory, following a single-surface, rate-independent, non-associated formulation. Density also changes as a function of porosity (Figure 14). A key feature of the critical state model is the incorporation of both mean and differential stress to compaction. In other words, porosity evolves during the simulation because of deposition, salt loading, and tectonic shortening. Because at shallow depths the horizontal stress in a salt column is higher than the uniaxial horizontal stress of sediments at the same depth (Heidari *et al.* 2017), a salt diapir loads sediments laterally. A key difference from commonly used basin models is that salt deforms the wall rocks and physically widens, when sediments deform plastically. In this case, sediment-layer line lengths are not being preserved, the salt diapir can upbuild through the roof and/or flow laterally within sediments, and the shape of the salt structure may not be dictated by the relative magnitudes of sedimentation and salt-rise rates (Nikolinakou *et al.* 2017).

The evolutionary Elfen model is based on a quasi-static, finite-element formulation accompanied by an automated adaptive-remeshing technique (Peric & Crook 2004) that activates when the model reaches a threshold plastic strain of 0.7. When activated, the remeshing technique locally generates an increase of smaller elements. The model is drained (i.e., pore pressures are hydrostatic) and we assume a fully submerged basin, therefore, the stresses obtained from the model are effective stresses. The mesh is composed of unstructured rectangular elements with an initial size of 200 m and a minimum size of 80 m when re-meshed. In addition, geometric pinching allows the removal of very thin layers that would otherwise cause element distortion and numerical instabilities.

Model variants (MV)

A number of parameters control the basin and diapir evolution (e.g., shortening rates, temperature gradient, sedimentation rate, etc). Some of these parameters, like the presence of a basal structural high or the very high sedimentation rates for the Pliocene and Quaternary intervals, also have a high level of uncertainty. We built and ran further models using the same initial configuration as the BC model but changing one of these parameters at a time to assess its influence. The model variants are:

- MV1: we use a sigmoidal shortening rate (dashed line, Figure 4c) instead of the BC exponential shortening rate (solid line, Figure 4c), maintaining the same shortening magnitude of 5 Km and its timing.
- MV2: we remove the basal triangular feature representing the rotated fault block interpreted below the diapirs (Figure 3).
- MV3: we increase the temperature gradient of the basin from 31°C/km to 36°C/km.
- MV4: we extract the burial history and the initial salt thickness along a vertical location at the NW side of the basin (location Z; Figure 3). This model aims to reproduce the Western diapir and explore the effect of deposition history on the evolution of a salt diapir.
- MV5: we reduce the sedimentation rates for Pliocene and Quaternary from 620 and 700 m/Myr, respectively to 61m/Myr. The original values come from the extraction of the layer thicknesses from the kinematic restoration model. However, they are interpreted to be unrealistic. The new values for this model are more in line to the sedimentation rates for Oligocene and Miocene.

Table 1: Summary of evolutionary models.

	Name	Variable changed	Original value	Changed value
BASE-CASE	BC	…	…	…
SENSITIVITY ANALYSIS	MV1	Shortening rate	Exponential (Figure 4c)	Sigmoidal (Figure 4c)
	MV2	Basal geometry	With triangular shape	No triangular shape
	MV3	Temperature gradient	31 °C/km	36 °C/km
	MV4	Burial history	Figure 5a	Figure 5b
	MV5	Plio-Quaternary sed. rates	620 and 700 m/Myr	61 m/Myr

Table 2: Thickness and sea floor angles from sequential kinematic restoration model at the end of each geologic time interval.

Name	Duration (Myr)	Total thickness at end of stage (m)	Sea floor angle at end of stage (°)
Jurassic	52	4500	0.43
Lower Cretaceous	45	1270	0.32
Upper Cretaceous	34	1230	0.22
Paleocene/Eocene	32	1000	0.32
Oligocene	11	615	0.21
Miocene	17.1	1080	0.42
Pliocene	2.8	620	0.38
Present day	2.5	700	0.53

EVOLUTIONARY MODEL RESULTS

The prograding sediment wedge imposes a differential load on the salt layer. The resulting shear (differential) stress drives viscous salt flow. The average salt differential stress in the model varies between 0.05 and 1 MPa and is comparable with published values (e.g., Schléder & Urai, 2007). Despite its low value, this shear stress is able to mobilize the salt, given the salt's average viscosity. The relatively low strain rates and low upper crustal temperatures used in this study yield an average salt viscosity between 10^{17} to 10^{19} Pa·s, consistent with typical values reported for salt rocks (van Keken *et al.* 1993; Marketos *et al.* 2016; Hamilton-Wright *et al.* 2019b; Rowan *et al.* 2019).

Base-case model results (BC)

The deposition of the earliest Jurassic sediments results in a differential overburden load between the salt seed (initial salt dent; dashed circle in Figure 4a) and the topographic lows on the salt top surface, triggering the salt flow into a diapir (Figure 6a & b). Further Jurassic deposition drives salt from the source layer into the diapir, which widens and rises, reaching the surface at 145 Ma (Figure 6b). At this time, the upper half of the diapir is narrow compared to the lower half and the 6.5 km thick pedestal (triangular-shaped base connecting the diapir with the salt source layer; Vendeville & Nilsen, 1993). The thick pedestal allows salt to flow from the source layer into the diapir. At 123 Ma (Early Cretaceous, Figure 6c), the diapir morphology changes: the diapir remains at surface but the upper part has grown considerably wider relative to the previous time illustrated in Figure 6b. At 123Ma (Figure 6c), the salt pedestal is still wider than the diapir; however, the source layer has thinned significantly.

At 100 Ma (end of Early Cretaceous, Figure 6d), the source layer welds along both sides of the diapir, leaving the pedestal completely isolated. However, a significant volume of salt exists in the pedestal, which allows for the diapir to continue growing and for salt to flow on the basin surface. This forms a salt sheet downslope (salt breadth several times greater than its thickness; Jackson & Hudec, 2017) and an overhang upslope (enlarged periphery of the diapir crest; Jackson & Hudec, 2017; Figure 6d). In our case, the salt sheet developed downslope has a total breadth of approximately 8 km and a thickness of 2 km. Deposition of the Upper Cretaceous (100-66 Ma; Figure 6e) buries the salt. However, the diapir keeps rising and thickening the salt sheet by depleting salt from the pedestals and thinning the diapir stem (slender part of the salt diapir connecting its upper part with the pedestal; Jackson & Hudec, 2017). Further salt flow is facilitated by the regional shortening, which is activated during the Late Cretaceous stage. This shortening, which remains active to present day (Figure 6f & g), continues to narrow the diapir stem and to drive the salt upwards. In addition, it drives salt flow from the salt sheets towards the centre of the diapir. As a result, the diapir crest bulges upwards, despite the subsequent deposition of Paleocene to Quaternary layers.

MV1 results (Shortening rate)

There is evidence, in many salt basins, that salt flow can be driven by tectonic shortening (Vendeville & Nilsen 1995; Nilsen *et al.* 1996; Koyi 1998; Brun & Fort 2004; Dooley *et al.* 2009). Shortening is documented for the Tarfaya basin (Michard *et al.* 2008; Wenke *et al.* 2011; Tari & Jabour 2013) but the history and rate of deformation during shortening is not confidently known. In this model variant, we use a sigmoidal shortening curve (dashed line, Figure 4c) instead of the exponential shortening curve used in BC (solid line, Figure 4c) while maintaining the same timing and total magnitude of shortening (5 km). This sigmoidal shape does not greatly alter the kinematics of the salt diapir and its end geometry (Figure 7a & b), for the given shortening and deposition rates, and the timing of shortening application.

We do find, however, that the different shortening rates (Figure 4c) significantly impact the present-day stress state (Figure 8**,** also Figure 15, Appendix C). We use the horizontal-to-vertical effective stress ratio K (colour contours, Figure 8) to illustrate how stresses change compared to the uniaxial state (K_0=0.8, light blue colours, Figure 8). Effective stress-ratio values lower than 0.8 (darker blue colours) indicate a decrease in horizontal effective stress (σ'_h) relative to the vertical effective stress (σ'_v). K=1 (green colours, Figure 8) indicates a uniform stress state ($\sigma'_h = \sigma'_v$). K higher than 1 (warm colours, Figure 8) indicates that σ'_h is higher than σ'_v. In the BC model, the values of K are higher than 1.3 near the salt crest and around 1.2 at the salt flanks. Instead, in model VM1 the values of K near the salt crest are around 0.6 (below uniaxial), with uniaxial values at the salt flanks.

MV2 results (Basal triangular feature)

Regional seismic interpretation and regional constraints (Le Roy & Piqué 2001; Tari & Jabour 2013) indicate that both the Sandia and the Western diapirs developed over the highest points of rotated fault blocks (Figure 3). However, seismic image quality below salt in this area is poor and the presence of this basal high cannot be confirmed. We investigate whether salt-base highs have a notable effect on the evolution of the diapir by replacing the basal indentation present in the BC model (Figure 7a) with a flat salt base in MV2 model (Figure 7c). The general characteristics of the resulting diapir in MV2 are similar to the BC one: the diapir rises early during the deposition of Jurassic sediments, a salt sheet develops downslope during the Early Cretaceous and the source layer welds at both sides of the diapir pedestal at the same interval. However, the diapir at MV2 reaches the surface earlier than the BC diapir and has a thicker upper part at the end of Jurassic. At Early Cretaceous time, the diapir expands and forms shorter salt sheets at both sides. The burial of the structure happens shortly after that time, contrary to the BC model, where the salt is completely buried at 101 Ma (beginning of Late Cretaceous). The final diapir geometry in MV2 is 400 m shorter and with a salt stem twice as thick compared to the BC diapir (Figure 7a & c).

MV3 results (Temperature)

The temperature gradient present in the basin affects the viscosity of the salt. The 31°C/km gradient used in the BC model is a lower bound for the study area (Rimi 2001; Zarhloule *et al.* 2010) based on an integrated 2D and 3D petroleum system model for thermal maturity evaluation. We investigate the effect of increasing the temperature gradient to 36°C/km on the evolution of the salt diapir and its final geometry (model MV3; Figure 7d). The resulting diapir rises during the Jurassic and generates a salt sheet during Early Cretaceous times, similar to the BC model. The source layer also welds during Early Cretaceous. The main effect of the higher temperature gradient in model MV3 is that the diapir upbuilds to the surface before the end of Jurassic, faster than the BC diapir (Figure 6b), and has a wider upper half. This small increase in salt-flow velocity results from the fact that the salt viscosity is at most an order of magnitude lower in the MV3 compared to the BC model (10^{17} and 10^{18} Pa·s), because of the higher temperature. The lateral expansion of the upper half part of the diapir starts at 131 Ma (Early Cretaceous) and generates a shorter salt sheet at the NW side and a shorter overhang at the SE at 122 Ma (Early Cretaceous). The structure is buried by ongoing sedimentation just after the formation of the salt sheet and overhang. The final diapir geometry in model MV3 is 600 m shorter and with a salt stem twice as thick compared to the BC diapir (Figure 7a & d).

MV4 results (Western diapir)

According to the kinematic restoration model, Jurassic and Cretaceous times have a higher sedimentation rate at location Z (basinward part of the studied cross section; Figure 3), relative to location Y. This higher sedimentation rates imply a larger accommodation space, hence larger volume of salt withdrawal at the basinward end of the basin. To explore this, we build the evolutionary model MV4 using the burial history (Figure 5b) along location Z in the kinematic restoration model (Figure 3) with a thicker initial salt layer (Figure 9a).

Similar to model BC, the deposition of the first Jurassic sediments in model MV4 results in a differential overburden stress between the salt seed and the topographic lows on the salt top surface, initiating salt flow toward the diapir (Figure 9a & b). The subsequent deposition of Jurassic layers drives the salt from the source layer into the diapir. The fast deposition (Figure 5b) allows the diapir to upbuild to the surface at 158 Ma, before the end of Jurassic (Figure 9b). At this time, the upper diapir half is narrower than its lower half and pedestal. At 135 Ma (Early Cretaceous, Figure 9c) the salt source layer is significantly thinned at both sides of the diapir. The upper half of the salt structure remains at the surface and has grown wider and developed overhangs at both sides. The sedimentation of Early Cretaceous partially buries these overhangs, limiting their lateral extension. By 100 Ma (Figure 9d), Lower Cretaceous sediments have buried the diapir. However, a significant volume of salt remains in the pedestals, and continues to drive salt flow to the upper parts of the diapir. As a result, the diapir crest inflates and the overhangs continue to grow. The onset of regional shortening (Figure 4c, solid curve) during Late Cretaceous (66 Ma; Figure 9e) both narrows the diapir stem and drives salt from the overhangs toward the upper diapir. This inward and upward salt-flow volume is sufficient to sustain a gradual rise of the diapir through the sedimentary roof. Salt eventually upbuilds to the present-day surface at 5 Ma (Figure 9g).

MV5 results (Plio-Quaternary sedimentation rates)

The sedimentation rates extracted from the kinematic restoration model at location Y (Figure3) present very high values of 620 and 700 m/Myr for the time intervals of Pliocene and Quaternary, respectively (light yellow and gray blocks, Figure 10). We use the model MV5 to reduce the Plio-Quaternary sedimentation rates to equal the value of the Miocene rate (61m/Myr, yellow block, Figure 10). The resulting present-day geometry of the basin in the model MV5 is not notably different from the BC model. This is because the duration of the Plio-Quaternary interval is short (5.3 Myr). Despite the high sedimentation rates, the sediment layer thicknesses are small, and the additional overburden load does not produce any notable effect on the kinematics of the system.

DISCUSSION

The role of sedimentation rate on diapir evolution

Sedimentation rates of the Tarfaya basin are a key driver for the system evolution. The rapid sedimentation at the beginning of the simulation (Jurassic) mobilizes the salt from the source layer towards the central part of the basin. We quantify the effect of sedimentation on salt flow by plotting the salt horizontal pressure gradient (Figure 11). We calculate this gradient by subtracting the sediment overburden load on salt away from the diapir from the salt pressure inside the diapir at the same depth (Figure 11-inset). The salt gradient increases rapidly during the Jurassic (blue line, Figure 11), illustrating the acceleration of salt flow towards the diapir. As a result, by the end of the Jurassic interval (at 145 Ma), the diapir has upbuilt to the sea floor and a significant volume of salt has accumulated in the salt pedestals (Figure 6b). Salt in this broad pedestal area further maintains the diapir rise during the Cretaceous interval, despite decrease in sedimentation rates (87 m/Myr during Jurassic, blue block in Figure 10 vs. 30 m/Myr during Cretaceous, dark and light green blocks in Figure 10).

The evolution of model MV4 (Figure 9) further illustrates the importance of the sedimentation rates in the diapir evolution. In this model, the higher sedimentation rates during Jurassic result in a higher horizontal pressure gradient in the salt source layer (green vs. blue line, Figure 11). This promotes a faster salt flow, and a greater amount of salt pumped into the MV4 diapir, despite the fact that the source layer in MV4 welds much earlier than the one in the BC model. As a result, salt in MV4 not only accumulates in the pedestals and upbuilds to the sea floor, but also forms diapir overhangs (Figure 9d). This geometry allows additional salt volume to be stored in the diapir and be readily available to flow in response to the later-applied shortening. As a result, the system is able to sustain a second phase of diapir rise to the present-day sea floor. Contrary to MV4 diapir, the BC diapir gets buried during Cretaceous times (Figure 6e) because a sufficient salt volume could not be mobilized.

Comparison of layer thicknesses estimated by kinematic restoration and predicted by evolutionary geomechanical model

Kinematically-constrained geomechanical models, such as that presented here, incorporate the strength and deformation characteristics of sediments in the study of a salt-basin evolution. We demonstrate this contribution by comparing the layer thicknesses from the BC model against the kinematic restoration model at: (a) location close to the diapir, near the tip of the source-layer weld (locations X and C, Figure 3 & 6, respectively); (b) location far from the diapir, above a salt high, where the salt source layer is not depleted (locations Y and A, same as the location used to constrain the evolutionary model; Figure 3 & 6, respectively). Whereas both approaches predict the same thicknesses away from the diapir (solid shapes in Figure 12 fall on the 1:1 line), the geomechanical model predicts 20% thicker layers closer to the diapir (empty shapes in Figure 12 fall around the 1:1.2 line).

We perform this comparison for the Jurassic, Cretaceous and Oligocene sediments (colours blue, green and orange in Figure 12, respectively) and for the time intervals of Late Cretaceous, Oligocene and present day (triangle, circle and square shapes in Figure 12, respectively). Consider, for example, the Jurassic sediments (blue shapes). Near the salt structure (empty shapes), at the end of Late Cretaceous (empty blue triangle, Figure 12), the restoration model provides a thickness of 4300 m, whereas the evolutionary model predicts 5000 m. The same is true for the Upper Cretaceous and Oligocene sediments (empty green and orange markers, respectively, Figure 12). These differences are associated with the depletion of the salt source layer and the formation of a salt weld during Cretaceous and highlight the importance of modeling the viscous salt flow and its response to sediment loading.

In addition, the geomechanical model predicts a notably higher compaction of the Jurassic layer between Late Cretaceous and present day (empty blue square, Figure 12): the final evolutionary model thickness is 4600 m (8% compaction), compared to 4200 m (2.3% compaction) in the restoration model. The source-layer weld generates higher mean stresses near the tip and a zone of higher shear stress that radiates upwards from the weld (Heidari *et al.* 2016).The geomechanical model captures this contribution of mean and shear stress to compression, because it simulates sediments as porous elasto-plastic material. This additional sediment compaction cannot be accounted for in the restoration model.

Influence of shortening rates on stress distribution

The geomechanical model provides the stress distribution around the salt structures resulting from the system evolution. This allows us to study the influence of shortening rates on the present-day stress state near the Sandia diapir (Figure 8).

The exponential shortening curve (solid black line, Figure 4c) applied in the BC model (Figure 8a) results in an active regional compressive load at present day, which pressurizes the diapir salt. Because of the overburden thickness, the crest cannot expand, and instead loads the sediments around it. As a result, the stress ratio increases to values near 1 at the salt flanks (green/yellow contour colours, Figure 8a), and to K=1.4 around the crest (orange contour colours, Figure 8a), illustrating increase in horizontal stress compared to its uniaxial value (K_0 = 0.8).

In contrast, the sigmoidal shortening curve (dashed black line, Figure 4c) applied in model MV1 (Figure 8b) results in decreasing shortening rates toward the end of the simulation and termination of shortening 2 Myr before present day. Because there is no active tectonic load, the diapir deforms downward and outward to achieve a uniform stress state (Hooghvorst *et al.* 2020). Consequently, the stress ratio at the crest decreases to values of K near 0.65, indicating decrease in horizontal stress (Figure 8b). Measurements in the Sandia-1 exploratory well (black circle, Figure 1) drilled in 2015 (Fernandez *et al.* 2015) show stress reduction above the Sandia diapir, indicating that a sigmoidal curve is more appropriate for this basin.

Parameters with minor influence on the Tarfaya basin evolution

Despite the importance of shortening rates on the final stress state, they have minor effect on the final salt geometry (Figure 7 BC vs. MV1 models; solid vs. dashed line, Figure 4c). This is because shortening begins during the Late Cretaceous, whereas the salt system mainly develops between Jurassic and Late Cretaceous. The role of shortening is better highlighted in the Western diapir (MV4) model. In this case, because of the higher salt volume accumulated in the diapir, overhang, and pedestal areas, the application of shortening is able to drive the salt to the present-day seafloor. The timing of shortening application, as well as the relative deposition and shortening rates affect the role of shortening in basin and diapir evolution.

The presence or absence of the salt-base high does not greatly impact the evolution or final geometry of the diapir (BC model, Figure 7a vs. MV2 model, Figure 7c). However, salt flows easier into the MV2 diapir in the absence of a rotated fault block feature at the salt base (Figure 7c), causing an earlier maturation of the structure. In addition, the salt source layer welds at an earlier time (nearly 20 Myr earlier than BC model), preventing the diapir to rise further and generating a shorter, wider structure. In contrast, the presence of a salt-base high (BC model, Figure 7a) delays the diapir rise. It should be noted that a salt-base high may play a key role in focusing salt flow into a structure, whereas in both models the diapir location is predefined with a seed in the initial geometry (Figure 4a).

Increase in temperature gradient in the salt does not greatly change the overall evolution or the final diapir geometry either (BC model, Figure 7a vs. MV3 model, Figure 7d). The temperature increase causes the salt viscosity to decrease, which facilitates salt flow into the diapir during Jurassic. This causes the diapir at MV2 to evolve faster, reaching the surface and welding the salt source layer at earlier times compared to the BC model. The resulting salt structure matures earlier, being buried by sediments during the Early Cretaceous, compared to the BC diapir that is buried during the Late Cretaceous. The final MV2 diapir geometry (Figure 7d) is shorter and wider compared to the BC structure (Figure 7a).

MODELLING UNCERTAINTIES AND LIMITATIONS

The evolutionary models built in this study simplify the Atlas inversion and shortening into a continuous curve that extends from Late Cretaceous until the present day (Figure 4c). However, Atlasic shortening most probably happened in distinct pulses (Fraissinet *et al.* 1988; Görler *et al.* 1988; El Harfi *et al.* 1996, 2001; Frizon de Lamotte *et al.* 2000).

The simulations in this study are 2-dimensional plane-strain models. They cannot account for any out-of-plane salt flow and require a wider source layer for the interpreted initial salt thickness. Hence, they overestimate the lateral extent of source-layer withdrawal during the diapir rise. The models also simulate a salt wall, whereas Sandia diapir geometry is closer to a dome (Hooghvorst *et al.* 2020). Evolutionary 3D models would represent more accurately the Tarfaya salt basin – but they are difficult to constrain and expensive to run.

Model input for the sediments has not been calibrated specifically for the study area, but it provides a good approximation of compressibility and strength for marine deposits (e.g., Nikolina*kou et al.* 2018b; Heidari *et al.* 2019). The constitutive formulation does not account for strain softening of faulting. As a result, differential stresses may be unrealistically high in locations where faults would otherwise form.

Sediment geology has been simplified to a single shale lithology. Data from wells drilled on the continental shelf Cap Juby-1 well (black triangle, Figure 1) indicate the presence of carbonates between the Jurassic sediments; however, it is not clear whether such layers exist in the basinward location of the study area.

All models in this study are drained and do not model the generation of overpressures. Overpressures would prevent compression and reduce the accommodation space for each deposition stage (Swarbrick *et al.* 2002; Nikolinakou *et al.* 2018a; Heidari *et al.* 2019). In addition, overpressures would decrease the strength of mudrocks by keeping the effective stress low, hence play a key role in the kinematics of the salt flow (Nikolinakou *et al.* 2018a).

Despite these limitations, this study is one of the first efforts to incorporate the geologic constraints provided by a sequential kinematic restoration model into an evolutionary geomechanical model of a salt basin.

CONCLUSIONS

We use burial history, sea floor geometry and tectonic loading extracted from a sequential kinematic restoration model to constrain a 2D geomechanical forward model and reproduce the evolution of the Sandia diapir (Tarfaya basin, NW African coast). The resulting final geometry of the geomechanical model is comparable with the present-day interpretation of the Sandia diapir. We find that sedimentation rates are a key driver for the halokinetic evolution of the system: higher rates at the early stages of the salt-diapir formation affect whether the diapir will get buried or upbuild to the sea floor, when the Atlas shortening is introduced later in the basin history. We also find that shortening-rate histories significantly affect the present-day stress state above the Sandia diapir: a sigmoidal shortening curve leads to a decrease in horizontal stresses above the crest of the structure, which is in agreement with field observations from an exploratory well.

More broadly, we show that incorporation of burial and tectonic histories from a sequential kinematic restoration leads to more realistic evolutionary geomechanical models that predict interpreted present-day geometries of geologic structures and help illuminate the key drivers of their structural evolution. In turn, geomechanical models incorporate the mechanical interaction between salt and sediments and can provide valuable information on the evolution of stress, porosity and potentially pore pressure with time, ultimately providing a more complete picture of the basin history.

Data Availability Statement

The data that support the findings of this study are available from the corresponding author upon reasonable request.

Acknowledgments

We are grateful to Repsol for granting access to the data of this study and for funding this work. We thank Pablo Hernandez for his contribution on building the sequential kinematic restoration model. We thank the UT GeoFluids consortium for their funding and continuous investment in this project. We sincerely thank Prof. Thigpen and Prof. Urai for their constructive criticism and review of the manuscript. We would also like to thank Rockfield for their support in the modelling using ELFEN licences and their help solving software-related doubts and numerical issues.

REFERENCES

Adachi, J., Nagy, Z.R., Sayers, C.M., Smith, M. & Becker, D.F. 2012. Drilling Adjacent to Salt Bodies: Definition of Mud Weight Window and Pore Pressure Using Numerical Models and Fast Well Planning Tool. *SPE Annual Technical Conference and Exhibition*, 1–11, https://doi.org/10.2118/159739-MS.

Albertz, M. & Beaumont, C. 2010. An investigation of salt tectonic structural styles in the Scotian Basin, offshore Atlantic Canada: 2. Comparison of observations with geometrically complex numerical models. *Tectonics*, **29**, n/a-n/a, https://doi.org/10.1029/2009TC002540.

Beaumont, C., Muñoz, J.A., Hamilton, J. & Fullsack, P. 2000. Factors controlling the Alpine evolution of the central Pyrenees inferred from a comparison of observations and geodynamical models. *Journal of Geophysical Research: Solid Earth*, **105**, 8121–8145, https://doi.org/10.1029/1999JB900390.

Ben-Awuah, J., Adda, G.W., Mijinyawa, A., Andriamihaja, S. & Siddiqui, N. 2013. 2D Basin modelling and petroleum system analysis of the triassic play in the hammerfest basin of the norwegian barents sea. *Research Journal of Applied Sciences, Engineering and Technology*, **6**, 3137–3150, https://doi.org/10.19026/rjaset.6.3615.

Bolas, H.M.N., Hermanrud, C. & Teige, G.M.G. 2004. Origin of overpressures in shales : Constraints from basin modeling. *AAPG Bulletin*, **88**, 193–211, https://doi.org/10.1306/10060302042.

Brun, J.-P. & Fort, X. 2004. Compressional salt tectonics (Angolan margin). *Tectonophysics*, **382**, 129–150, https://doi.org/10.1016/j.tecto.2003.11.014.

Carracedo, J.C. & Perez-Torrado, F.J. 2013. *Teide Volcano*. Carracedo, J. C. & Troll, V. R. (eds). Berlin, Heidelberg, Springer Berlin Heidelberg, Active Volcanoes of the World, https://doi.org/10.1007/978-3-642-25893-0.

Corti, G. & Dooley, T.P. 2015. Lithospheric-scale centrifuge models of pull-apart basins. *Tectonophysics*, **664**, 154–163, https://doi.org/10.1016/j.tecto.2015.09.004.

Crook, A.J.L., Willson, S.M., Yu, J.G. & Owen, D.R.J. 2006. Predictive modelling of structure evolution in sandbox experiments. **28**, 729–744, https://doi.org/10.1016/j.jsg.2006.02.002.

Crook, A.J.L., Obradors-Prats, J., Somer, D., Peric, D., Lovely, P. & Kacewicz, M. 2018. Towards an integrated restoration/forward geomechanical modelling workflow for basin evolution prediction. *Oil & Gas Sciences and Technology – Revue d'IFP Energies nouvelles*, **73**, 19, https://doi.org/10.2516/ogst/2018018.

Davison, I. 2005. Central Atlantic margin basins of North West Africa: Geology and hydrocarbon potential (Morocco to Guinea). *Journal of African Earth Sciences*, **43**, 254–274, https://doi.org/10.1016/j.jafrearsci.2005.07.018.

Dietl, C. & Koyi, H. 2011. Sheets within diapirs - Results of a centrifuge experiment. *Journal of Structural Geology*, **33**, 32–37, https://doi.org/10.1016/j.jsg.2010.10.010.

Dooley, T.P. & Hudec, M.R. 2017. The effects of base-salt relief on salt flow and suprasalt deformation patterns - Part 2: Application to the eastern Gulf of Mexico. *Interpretation*, **5**, SD25-SD38, https://doi.org/10.1190/INT-2016-0088.1.

Dooley, T.P. & Schreurs, G. 2012. Analogue modelling of intraplate strike-slip tectonics: A review and new experimental results. *Tectonophysics*, **574**–**575**, 1–71, https://doi.org/10.1016/j.tecto.2012.05.030.

Dooley, T.P., Jackson, M.P.A. & Hudec, M.R. 2009. Inflation and deflation of deeply buried salt stocks during lateral shortening. *Journal of Structural Geology*, **31**, 582–600, https://doi.org/10.1016/j.jsg.2009.03.013.

Dooley, T.P., Jackson, M.P.A. & Hudec, M.R. 2015. Breakout of squeezed stocks: Dispersal of roof fragments, source of extrusive salt and interaction with regional thrust faults. *Basin Research*, **27**, 3–25, https://doi.org/10.1111/bre.12056.

Dooley, T.P., Hudec, M.R., Carruthers, D., Jackson, M.P.A. & Luo, G. 2017. The effects of base-salt relief on salt flow and suprasalt deformation patterns - Part 1: Flow across simple steps in the base of salt. *Interpretation*, **5**, SD1-SD23, https://doi.org/10.1190/INT-2016-0087.1.

Durand-Riard, P., Shaw, J.H., Plesch, A. & Lufadeju, G. 2013. Enabling 3D geomechanical restoration of strike- and oblique-slip faults using geological constraints , with applications to the deep-water Niger Delta. *Journal of Structural Geology*, **48**, 33–44, https://doi.org/10.1016/j.jsg.2012.12.009.

Dusseault, M.B., Maury, V. & Sanfilippo, F. 2004. Drilling Around Salt : Stresses , Risks , Uncertainties. *Stress The International Journal on the Biology of Stress*.

El Harfi, A., Lang, J. & Salomon, J. 1996. Cenozoic continental infilling of the Ouarzazate foreland basin. Implications for the structural evolution of the Central High Atlas Mountains (Morocco). *Comptes Rendus de l'Academie de Sciences - Serie IIa: Sciences de la Terre et des Planetes*, **323**, 623–630.

El Harfi, A., Lang, J., Salomon, J. & Chellai, E.H. 2001. Cenozoic sedimentary dynamics of the Ouarzazate foreland basin (Central High Atlas Mountains, Morocco). *International Journal of Earth Sciences*, **90**, 393–411, https://doi.org/10.1007/s005310000115.

Farzipour-Saein, A. & Koyi, H. 2014. Effect of lateral thickness variation of an intermediate decollement on the propagation of deformation front in the Lurestan and Izeh zones of the Zagros fold-thrust belt, insights from analogue modeling. *Journal of Structural Geology*, **65**, 17–32, https://doi.org/10.1016/j.jsg.2014.03.004.

Fernandez, N. & Kaus, B.J.P. 2015. Pattern formation in 3-D numerical models of down-built diapirs initiated by a Rayleigh–Taylor instability. *Geophysical Journal International*, **202**, 1253–1270, https://doi.org/10.1093/gji/ggv219.

Fernandez, O., Harrold, T., Ferguson, W., Gonzalez, H. & Bere, A. 2015. Three-dimensional Prediction of Stress Distribution Above a Salt Diapir - Application to a Deepwater Hydrocarbon Exploration Well. *In*: *77th EAGE Conference and Exhibition 2015: Earth Science for Energy and Environment*. 965–969., https://doi.org/10.3997/2214-4609.201412715.

Fraissinet, C., El Zouine, M., Morel, J., Poisson, A., Andrieux, J. & Faure-Muret, A. 1988. Structural evolution of the southern and northern Central High Atlas in paleogene and Mio-Pliocene times. *In*: Jacobshagen, V. H. (ed.) *The Atlas System of Morocco: Studies on Its Geodynamic Evolution*. Berlin, Heidelberg, Springer Berlin Heidelberg, 273–291., https://doi.org/10.1007/BFb0011597.

Fredrich, J.T., Coblentz, D., Fossum, A.F. & Thorne, B.J. 2003. Stress Perturbations Adjacent to Salt Bodies in the Deepwater Gulf of Mexico. *SPE Annual Technical Conference and Exhibition*, 5–8, https://doi.org/10.2118/84554-MS.

Fredrich, J.T., Fossum, A.F. & Hickman, R.J. 2007a. Mineralogy of deepwater Gulf of Mexico salt formations and implications for constitutive behavior. *Journal of Petroleum Science and Engineering*, **57**, 354–374, https://doi.org/10.1016/j.petrol.2006.11.006.

Fredrich, J.T., Engler, B.P., Smith, J.A., Onyia, E.C. & Tolman, D.N. 2007b. Predrill Estimation of Subsalt Fracture Gradient: Analysis of the Spa Prospect to Validate Nonlinear Finite Element Stress Analyses. *SPE/IADC Drilling Conference*, 8, https://doi.org/10.2118/105763-MS.

Frizon de Lamotte, D., Saint Bezar, B., Bracène, R. & Mercier, E. 2000. The two main steps of the Atlas building and geodynamics of the western Mediterranean. *Tectonics*, **19**, 740–761, https://doi.org/10.1029/2000TC900003.

Frizon de Lamotte, D., Zizi, M., et al. 2008. The Atlas System. *In*: Otto, J.-C. & Dikau, R. (eds) *Continental Evolution: The Geology of Morocco*. Berlin, Heidelberg, Springer Berlin Heidelberg, 133–202., https://doi.org/10.1007/978-3-540-77076-3_4.

Görler, K., Helmdach, F.-F., et al. 1988. The uplift of the central High Atlas as deduced from neogene continental sediments of the Ouarzazate province, Morocco BT - The Atlas System of Morocco: Studies on its Geodynamic Evolution. *In*: Jacobshagen, V. H. (ed.). Berlin, Heidelberg, Springer Berlin Heidelberg, 359–404., https://doi.org/10.1007/BFb0011601.

Goteti, R., Ings, S.J. & Beaumont, C. 2012. Development of salt minibasins initiated by sedimentary topographic relief. *Earth and Planetary Science Letters*, **339**–**340**, 103–116, https://doi.org/10.1016/j.epsl.2012.04.045.

Gouiza, M. 2011. *Mesozoic Source-to-Sink Systems in NW Africa: Geology of Vertical Movements during the Birth and Growth of the Moroccan Rifted Margin: Ph.D Thesis*. VU University Amsterdam.

Gradmann, S. & Beaumont, C. 2012. Coupled fluid flow and sediment deformation in margin-scale salt-tectonic systems: 2. Layered sediment models and application to the northwestern Gulf of Mexico. *Tectonics*, **31**, 1–22, https://doi.org/10.1029/2011TC003035.

Gradmann, S., Beaumont, C. & Ings, S.J. 2012. Coupled fluid flow and sediment deformation in margin-scale salt-tectonic systems: 1. Development and application of simple, single-lithology models. *Tectonics*, **31**, 1–17, https://doi.org/10.1029/2011TC003033.

Gutierrez, M. & Wangen, M. 2005. Modeling of compaction and overpressuring in sedimentary basins. *Marine and Petroleum Geology*, **22**, 351–363, https://doi.org/10.1016/j.marpetgeo.2005.01.003.

Hamilton-Wright, J., Dee, S., von Nicolai, C. & Johnson, H. 2019. Investigating controls on salt movement in extensional settings using finite element modelling. *Petroleum Geoscience*, **25**, 258–271, https://doi.org/10.1144/petgeo2018-119.

Hantschel, T. & Kauerauf, A. 2009. *Fundamentals of Basin and Petroleum Systems Modeling*. Berlin, Heidelberg, Springer Berlin Heidelberg, https://doi.org/10.1007/978-3-540-72318-9.

Heidari, M., Nikolinakou, M.A., Hudec, M.R. & Flemings, P.B. 2016. Tectonophysics Geomechanical analysis of a welding salt layer and its effects on adjacent sediments. *Tectonophysics*, **683**, 172–181, https://doi.org/10.1016/j.tecto.2016.06.027.

Heidari, M., Nikolinakou, M.A., Flemings, P.B. & Hudec, M.R. 2017. A simplified stress analysis of rising salt domes. *Basin Research*, **29**, 363–376, https://doi.org/10.1111/bre.12181.

Heidari, M., Nikolinakou, M.A. & Flemings, P.B. 2018. Coupling geomechanical modeling with seismic pressure prediction. *Geophysics*, **83**, B253–B267, https://doi.org/10.1190/geo2017-0359.1.

Heidari, M., Nikolinakou, M.A., Hudec, M.R. & Flemings, P.B. 2019. Influence of a reservoir bed on diapirism and drilling hazards near a salt diapir: A geomechanical approach. *Petroleum Geoscience*, **25**, 282–297, https://doi.org/10.1144/petgeo2018-113.

Hooghvorst, J.J., Harrold, T.W.D., Nikolinakou, M.A., Fernandez, O. & Marcuello, A. 2020. Comparison of stresses in 3D v. 2D geomechanical modelling of salt structures in the Tarfaya Basin, West African coast. *Petroleum Geoscience*, **26**, 36–49, https://doi.org/10.1144/petgeo2018-095.

Hubbert, M.K. 1937. Theory of scale models as applied to the study of geologic structures. *Geological Society of America Bulletin*, **48**, 1459–1520, https://doi.org/10.1130/GSAB-48-1459.

Hubbert, M.K. 1951. Mechanical basis for certain familiar geologic structures. *Bulletin of the Geological Society of America*, **62**, 355–372, https://doi.org/10.1130/0016-7606(1951)62[355:MBFCFG]2.0.CO;2.

Hudec, M.R. & Jackson, M.P.A. 2004. Regional restoration across the Kwanza Basin, Angola: Salt tectonics triggered by repeated uplift of a metastable passive margin. *AAPG Bulletin*, **88**, 971–990, https://doi.org/10.1306/02050403061.

Jackson, M.P.A. & Hudec, M.R. 2017. *Salt Tectonics. Principles and Practice*. Cambridge University Press.

Kaus, B.J.P., Steedman, C. & Becker, T.W. 2008. From passive continental margin to mountain belt: Insights from analytical and numerical models and application to Taiwan. *Physics of the Earth and Planetary Interiors*, **171**, 235–251, https://doi.org/10.1016/j.pepi.2008.06.015.

Koyi, H. 1997. Analogue modelling: From a qualitative to a quantitative technique - A historical outline. *Journal of Petroleum Geology*, **20**, 223–238, https://doi.org/10.1111/j.1747-5457.1997.tb00774.x.

Koyi, H. 1998. The shaping of salt diapirs. *Journal of Structural Geology*, **20**, 321–338, https://doi.org/10.1016/S0191-8141(97)00092-8.

Le Roy, P. & Piqué, A. 2001. Triassic-Liassic western Moroccan synrift basins in relation to the Central Atlantic opening. *Marine Geology*, **172**, 359–381, https://doi.org/10.1016/S0025-3227(00)00130-4.

Maerten, L. & Maerten, F. 2006. Chronologic modeling of faulted and fractured reservoirs using geomechanically based restoration : Technique and industry applications. *AAPG Bulletin*, **90**, 1201–1226, https://doi.org/10.1306/02240605116.

Marketos, G., Spiers, C.J. & Govers, R. 2016. Impact of rock salt creep law choice on subsidence calculations for hydrocarbon reservoirs overlain by evaporite caprocks. *Journal of*

Geophysical Research: Solid Earth, **121**, 4249–4267, https://doi.org/10.1002/2016JB012892.

Massoli, D., Koyi, H.A. & Barchi, M.R. 2006. Structural evolution of a fold and thrust belt generated by multiple décollements: analogue models and natural examples from the Northern Apennines (Italy). *Journal of Structural Geology*, **28**, 185–199, https://doi.org/10.1016/j.jsg.2005.11.002.

McGuinness, D.B. & Hossack, J.R. 1993. The Development of Allochthonous Salt Sheets as Controlled by the Rates of Extension, Sedimentation, and Salt Supply. *Rates of Geologic Processes, Tectonics, Sedimentation, Eustasy and Climate - Implications for Hydrocarbon Exploration: 14th Annual*, 127–139, https://doi.org/10.5724/gcs.93.14.0127.

McKenzie, D. 1978. Some remarks on the development of sedimentary basins. *Earth and Planetary Science Letters*, **40**, 25–32, https://doi.org/10.1016/0012-821X(78)90071-7.

Michard, A., Saddiqi, O., Chalouan, A. & Frizon de Lamotte, D. 2008. *Continental Evolution: The Geology of Morocco*. Otto, J.-C. & Dikau, R. (eds). Berlin, Heidelberg, Springer Berlin Heidelberg, Lecture Notes in Earth Sciences, https://doi.org/10.1007/978-3-540-77076-3.

Moretti, I. & Guiton, M.L.E. 2006. KINE3D : a New 3D Restoration Method Based on a Mixed Approach Linking Geometry and Geomechanics. *Oil & Gas Sciences and Technology – Revue d'IFP Energies nouvelles*, **61**, 277–289, https://doi.org/10.2516/ogst:2006021.

Munson, D.E. 1997. Constitutive model of creep in rock salt applied to underground room closure. *International journal of rock mechanics and mining sciences & geomechanics abstracts*, **34**, 233–247, https://doi.org/10.1016/S0148-9062(96)00047-2.

Munson, D.E. & Dawson, P.R. 1979. Constitutive model for the low temperature creep of salt (with application to WIPP). SAND79-1853. Sandia National Laboratories, Albuquerque, NM. 31.

Nikolinakou, M.A., Hudec, M.R. & Flemings, P.B. 2014. Comparison of evolutionary and static modeling of stresses around a salt diapir. *Marine and Petroleum Geology*, **57**, 537–545, https://doi.org/10.1016/j.marpetgeo.2014.07.002.

Nikolinakou, M.A., Heidari, M., Hudec, M.R. & Flemings, P.B. 2017. Initiation and growth of salt diapirs in tectonically stable settings: Upbuilding and megaflaps. *AAPG Bulletin*, **101**, 887–905, https://doi.org/10.1306/09021615245.

Nikolinakou, M.A., Heidari, M., Flemings, P.B. & Hudec, M.R. 2018a. Geomechanical modeling of pore pressure in evolving salt systems. *Marine and Petroleum Geology*, **93**, 272–286, https://doi.org/10.1016/j.marpetgeo.2018.03.013.

Nikolinakou, M.A., Flemings, P.B., Heidari, M. & Hudec, M.R. 2018b. Stress and Pore Pressure in Mudrocks Bounding Salt Systems. *Rock Mechanics and Rock Engineering*, **51**, 3883–3894, https://doi.org/10.1007/s00603-018-1540-z.

Nilforoushan, F. & Koyi, H.A. 2007. Displacement fields and finite strains in a sandbox model simulating a fold-thrust-belt. *Geophysical Journal International*, **169**, 1341–1355, https://doi.org/10.1111/j.1365-246X.2007.03341.x.

Nilsen, K.T., Johansen, J.-T. & Vendeville, B.C. 1996. Influence of Regional Tectonics on Halokinesis in the Nordkapp Basin , Barents Sea. *In*: Jackson, M. P. A., Roberts, D. G. & Snelson, S. (eds) *Salt Tectonics: A Global Perspective*. AAPG Memoir 65, 413–436.

Nygard, R., Gutierrez, M., Bratli, R.K. & Hoeg, K. 2006. Brittle-ductile transition, shear failure and leakage in shales and mudrocks. *Marine and Petroleum Geology*, **23**, 201–212.

Peric, D. & Crook, A.J.L. 2004. Computational strategies for predictive geology with reference to salt tectonics. **193**, 5195–5222, https://doi.org/10.1016/j.cma.2004.01.037.

Piqué, A., Le Roy, P. & Amrhar, M. 1998. Transtensive synsedimentary tectonics associated with ocean opening: The Essaouira-Agadir segment of the Moroccan Atlantic margin. *Journal of the Geological Society*, **155**, 913–928, https://doi.org/10.1144/gsjgs.155.6.0913.

Ramberg, H. 1981. The role of gravity in orogenic belts. *Geological Society Special Publication*, **9**, 125–140, https://doi.org/10.1144/GSL.SP.1981.009.01.11.

Reber, J.E., Cooke, M.L. & Dooley, T.P. 2020. What model material to use? A Review on rock analogs for structural geology and tectonics. *Earth-Science Reviews*, **202**, 103107, https://doi.org/10.1016/j.earscirev.2020.103107.

Rimi, A. 2001. Carte du gradient géothermique au Maroc. *Bulletin de l'institut scientifique, Rabat*, **23**, 1–6.

Rockfield. 2017. *Elfen Explicit Manual (Version 4.10)*. Software, R. (ed.). Swansea, UK.

Rowan, M.G. 1993. A systematic technique for the sequential restoration of salt structures. *Tectonophysics*, **228**, 331–348.

Rowan, M.G. & Ratliff, R.A. 2012. Cross-section restoration of salt-related deformation : Best practices and potential pitfalls. *Journal of Structural Geology*, **41**, 24–37, https://doi.org/10.1016/j.jsg.2011.12.012.

Rowan, M.G., Giles, K.A., Hearon, T.E. & Fiduk, J.C. 2016. Megaflaps adjacent to salt diapirs. *AAPG Bulletin*, **100**, 1723–1747, https://doi.org/10.1306/05241616009.

Rowan, M.G., Urai, J.L., Fiduk, J.C. & Kukla, P.A. 2019. Deformation of intrasalt competent layers in different modes of salt tectonics. *Solid Earth*, **10**, 987–1013, https://doi.org/10.5194/se-10-987-2019.

Schellart, W.P. & Strak, V. 2016. A review of analogue modelling of geodynamic processes: Approaches, scaling, materials and quantification, with an application to subduction experiments. *Journal of Geodynamics*, **100**, 7–32, https://doi.org/10.1016/j.jog.2016.03.009.

Schléder, Z. & Urai, J.L. 2007. Deformation and recrystallization mechanisms in mylonitic shear zones in naturally deformed extrusive Eocene-Oligocene rocksalt from Eyvanekey plateau and Garmsar hills (central Iran). *Journal of Structural Geology*, **29**, 241–255, https://doi.org/10.1016/j.jsg.2006.08.014.

Schreurs, G., Buiter, S.J.H., et al. 2016. Benchmarking analogue models of brittle thrust wedges. *Journal of Structural Geology*, **92**, 116–139, https://doi.org/10.1016/j.jsg.2016.03.005.

Sclater, J.G. & Christie, P.A.F. 1980. Continental stretching: An explanation of the Post-Mid-Cretaceous subsidence of the central North Sea Basin. *Journal of Geophysical Research: Solid Earth*, **85**, 3711–3739, https://doi.org/10.1029/JB085iB07p03711.

Segura, J.M., Matos da Cruz, A., Stachlewski, G., Alvarellos, J., Vargas, P.E. & Lakshmikantha, M.R.

2016. Fault stability assessment for well planning : a case study related to salt structures. *American Rock Mechanics Association. Paper 16-518*.

Stigall, J. & Dugan, B. 2010. Overpressure and earthquake initiated slope failure in the Ursa region, northern Gulf of Mexico. *Journal of Geophysical Research*, **115**, B04101, https://doi.org/10.1029/2009JB006848.

Swarbrick, R.E., Osborne, M.J. & Yardley, G.S. 2002. Comparision of Overpressure Magnitude Resulting from the Main Generating Mechanisms Generating Mechanisms. *AAPG Memoir*, **76**, 1–12.

Tari, G. & Jabour, H. 2013. Salt tectonics along the Atlantic margin of Morocco. *Geological Society, London, Special Publications*, **369**, 337–353, https://doi.org/10.1144/SP369.23.

Thibaut, M., Jardin, A., Faille, I., Willien, F. & Guichet, X. 2014. Advanced Workflows for Fluid Transfer in Faulted Basins. *Oil & Gas Science and Technology – Revue d'IFP Energies nouvelles*, **69**, 573–584, https://doi.org/10.2516/ogst/2014016.

Thigpen, J.R., Roberts, D., Snow, J.K., Walker, C.D. & Bere, A. 2019. Integrating kinematic restoration and forward finite element simulations to constrain the evolution of salt diapirism and overburden deformation in evaporite basins. *Journal of Structural Geology*, **118**, 68–86, https://doi.org/10.1016/j.jsg.2018.10.003.

Trudgill, B.D. & Rowan, M.G. 2004. Integrating 3D Seismic Data with Structural Restorations to Elucidate the Evolution of a Stepped Counter-Regional Salt System, Eastern Louisiana Shelf, Northern Gulf of Mexico. *Geological Society, London, Memoirs*, **29**, 165–176, https://doi.org/10.1144/GSL.MEM.2004.029.01.16.

van der Zee, W., Ozan, C., Brudy, M. & Holland, M. 2011. 3D geomechanical modeling of complex salt structures. *SIMULIA Customer Conference*, 1–16.

van Keken, P.E., Spiers, C.J., van den Berg, A.P. & Muyzert, E.J. 1993. The effective viscosity of rocksalt: implementation of steady-state creep laws in numerical models of salt diapirism. *Tectonophysics*, **225**, 457–476, https://doi.org/10.1016/0040-1951(93)90310-g.

Vendeville, B.C. & Nilsen, K. 1995. Episodic growth of salt diapirs driven by horizontal shortening.

In: *Salt, Sediment and Hydrocarbons*. Society of Economic Paleontologists and Mineralogists Gulf Coast Section, 285–295., https://doi.org/10.5724/gcs.95.16.0285.

Wenke, A., Zühlke, R., Jabour, H. & Kluth, O. 2011. High-resolution sequence stratigraphy in basin reconnaissance: Example from the Tarfaya Basin, Morocco. *First Break*, **29**, 85–96.

Willson, S.M., Fossum, A.F. & Fredrich, J.T. 2002. Assessment of Salt Loading on Well Casings. *Proceedings of the Drilling Conference*, 711–720, https://doi.org/10.2523/74562-ms.

Zarhloule, Y., Rimi, A., Boughriba, M., Barkaoui, A.E. & Lahrach, A. 2010. The Geothermal Research in Morocco : History of 40 Years. *In*: *World Geothermal Congress*.

Appendix A

Material laws and input properties

The salt creep behaviour is described by the following equations (Munson 1997). The transient term of the formulation is omitted, considered negligible over geological timescales. The list of parameters used are listed in Where ·εc is the salt viscosity, q is the shear stress, T is the temperature, R is the universal gas constant, μ is the shear modulus and A_1, A_2 n_1, n_2 are material constants.

Table 3.

$$\dot{\varepsilon}_c = A_1\left[\frac{q}{\mu}\right]^{n_1} e^{-Q_1/RT} + A_2\left[\frac{q}{\mu}\right]^{n_2} e^{-Q_2/RT} \qquad \text{(A1)}$$

$$\mu = \mu_0 - \frac{d\mu}{dT}(T - T_0) \qquad \text{(A2)}$$

Where $\dot{\varepsilon}_c$ is the salt viscosity, q is the shear stress, T is the temperature, R is the universal gas constant, μ is the shear modulus and A_1, A_2 n_1, n_2 are material constants.

Table 3: material properties for salt (Munson 1997; Fredrich *et al.* 2007a).

Parameter	Units	Value
E	MPa	10000
ν		0.35
ρ	kg/m3	2100
A_1	1/Myr	1.89E+39
n_1		5.5
Q_1	cal/mol	25000
A_2	1/Myr	2.17E+29
n_2		5
Q_2	cal/mol	10000
R	cal/°K/mol	1.987
T_0	°K	10
T_{const}	°K	273

μ_0	MPa	12400
$d\mu/dT$	MPa/°K	10

The sediment behaviour is represented by the constitutive SR3 model (Crook *et al.* 2006) that assumes an homogeneous, isotropic and porous elastoplastic material. At a high level, at each mechanical calculation step, the overall strain increment:

$$\Delta\varepsilon = \Delta\varepsilon_{\mathrm{e}} + \Delta\varepsilon_{\mathrm{p}} \quad \text{(A3)}$$

is coupled to the effective stress increment with the stiffness tensor D_T:

$$\Delta\sigma' = \mathrm{D_T}\Delta\varepsilon \quad \text{(A4)}$$

where σ' is the effective stress tensor, ε_e the elastic strain tensor and ε_p the plastic strain tensor.

Table 4: Material properties for sediments (Nygard *et al.* 2006; Rockfield 2017).

Parameter	Units	Value
$\mathbf{E_{ref}}$	MPa	40
v		0.25
$\mathbf{r_w}$	kg/m^3	1000
$\mathbf{r_s}$	kg/m^3	2700
k		0.01
$\mathbf{p_{t,0}}$	MPa	0.085
$\mathbf{p_{c,0}}$	MPa	-1
b	°	60
θ	°	51
$\mathbf{b_0}$		0.6
$\mathbf{b_1}$	1/Mpa	0.725
a		0.25
N		1.3
$\mathbf{n_0}$		0.38
Hardening properties	Figure 13	

Appendix B

Nomenclature

Table 5: Nomenclature.

Symbol	**Name**	**Dimensions**
σ'_v	Vertical effective stress	$L^{-1}M^1T^{-2}$
σ'_h	Horizontal effective stress	$L^{-1}M^1T^{-2}$
u_h	Hydrostatic pore pressure	$L^{-1}M^1T^{-2}$
K	Horizontal-to-vertical effective stress ratio	$L^0M^0T^{-0}$

Appendix C

Stress profiles at diapir crest

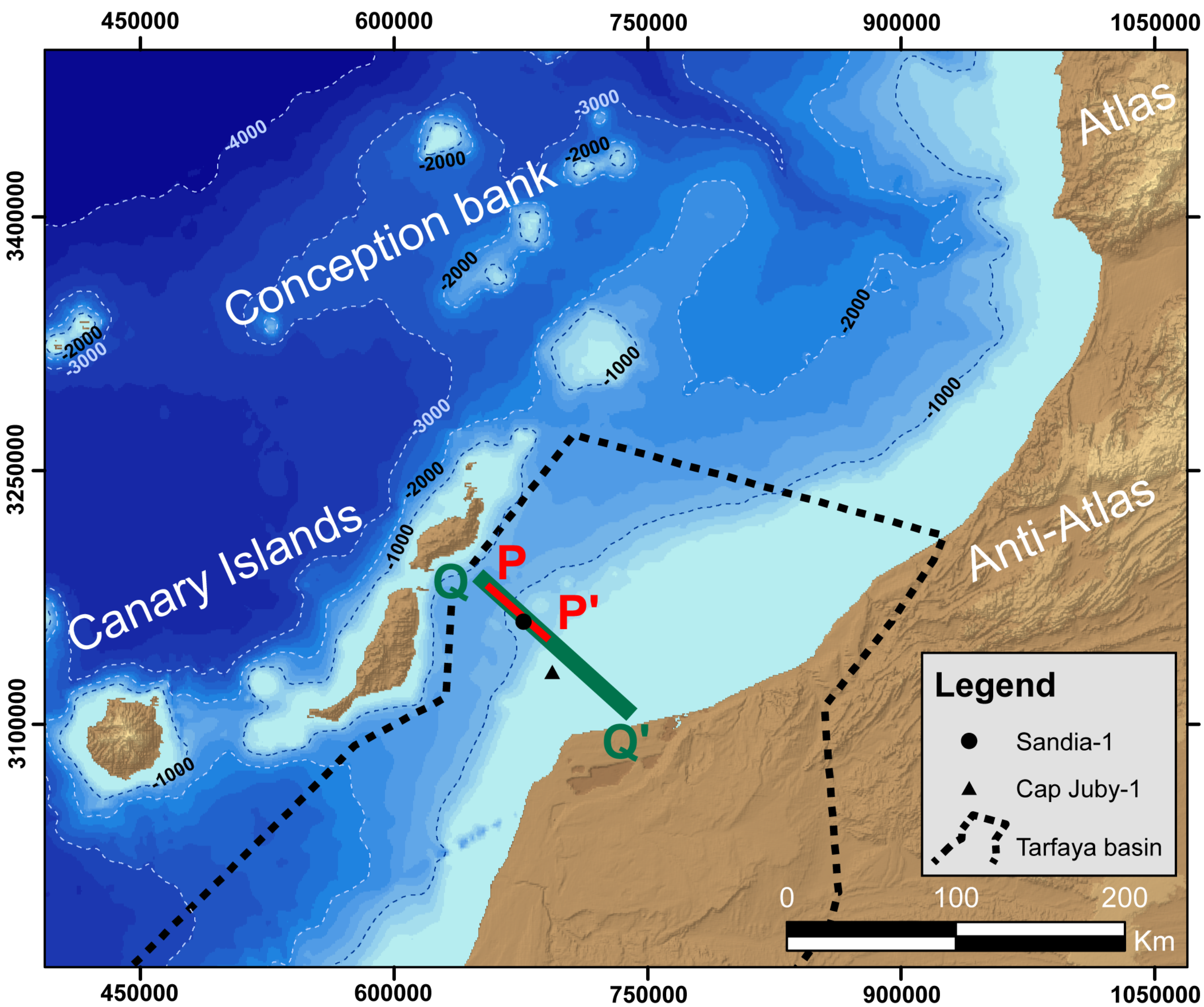

450000
600000
750000
900000
1050000
3400000
3250000
3100000
Conception bank
Canary Islands
Atlas
Anti-Atlas
-4000
-3000
-2000
-1000
P
P'
Q
Q'
Legend
Sandia-1
Cap Juby-1
Tarfaya basin
0
100
200
Km

Figure 1

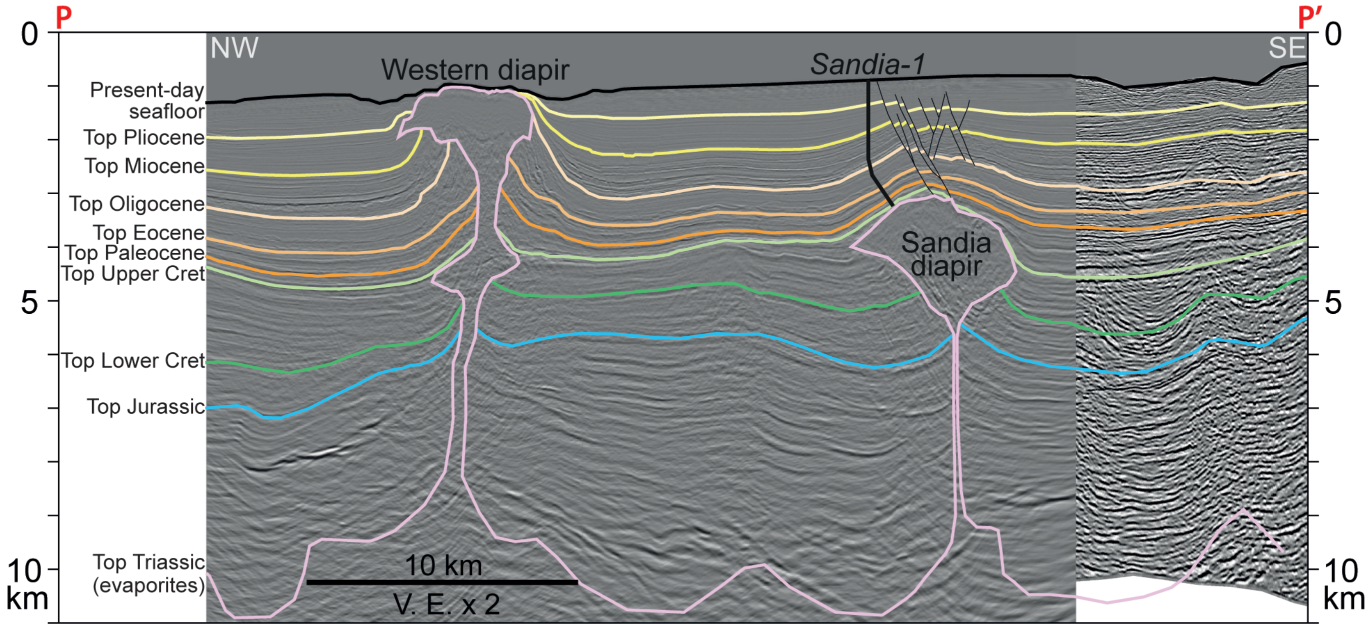

P
P'
0
5
10
km
NW
SE
Western diapir
Sandia-1
Present-day seafloor
Top Pliocene
Top Miocene
Top Oligocene
Top Eocene
Top Paleocene
Top Upper Cret
Top Lower Cret
Top Jurassic
Top Triassic (evaporites)
Sandia diapir
10 km
V. E. x 2

Figure 2

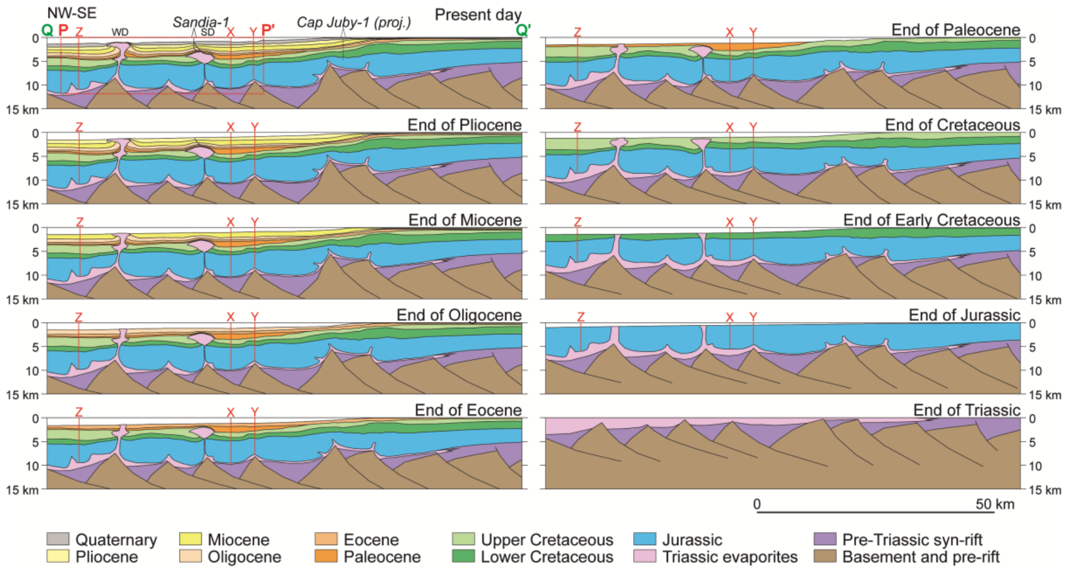
NW-SE
Present day
Q
P
Z
WD
Sandia-1
SD
X
Y
P'
Cap Juby-1 (proj.)
Q'
End of Paleocene
End of Pliocene
End of Cretaceous
End of Miocene
End of Early Cretaceous
End of Oligocene
End of Jurassic
End of Eocene
End of Triassic
0
5
10
15 km
0
50 km
Quaternary
Pliocene
Miocene
Oligocene
Eocene
Paleocene
Upper Cretaceous
Lower Cretaceous
Jurassic
Triassic evaporites
Pre-Triassic syn-rift
Basement and pre-rift

Figure 3

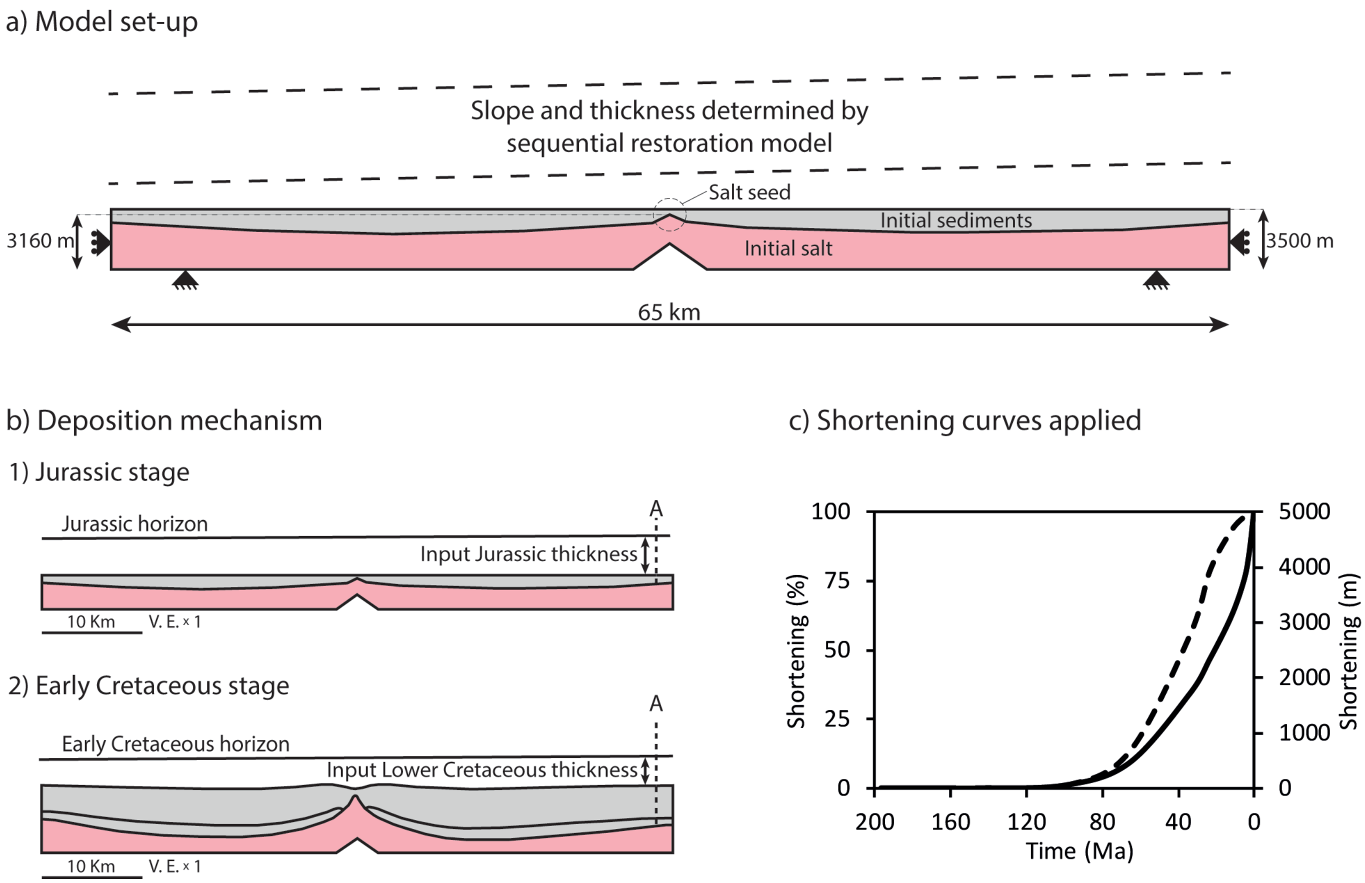

a) Model set-up
Slope and thickness determined by sequential restoration model
Salt seed
Initial sediments
Initial salt
3160 m
3500 m
65 km
b) Deposition mechanism
1) Jurassic stage
A
Jurassic horizon
Input Jurassic thickness
10 Km
V. E. × 1
2) Early Cretaceous stage
A
Early Cretaceous horizon
Input Lower Cretaceous thickness
10 Km
V. E. × 1
c) Shortening curves applied
100
75
50
25
0
Shortening (%)
5000
4000
3000
2000
1000
0
Shortening (m)
200
160
120
80
40
0
Time (Ma)

Figure 4

(a) Burial history diagram at location Y

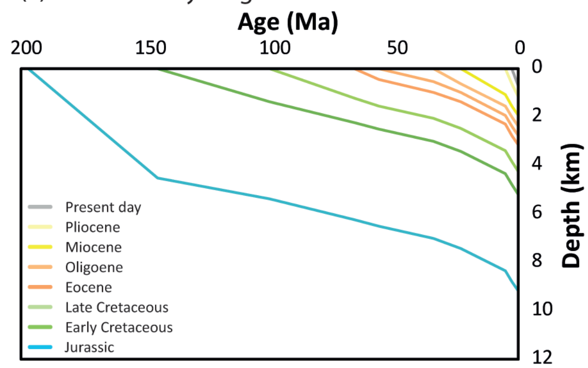

(b) Burial history diagram at location Z

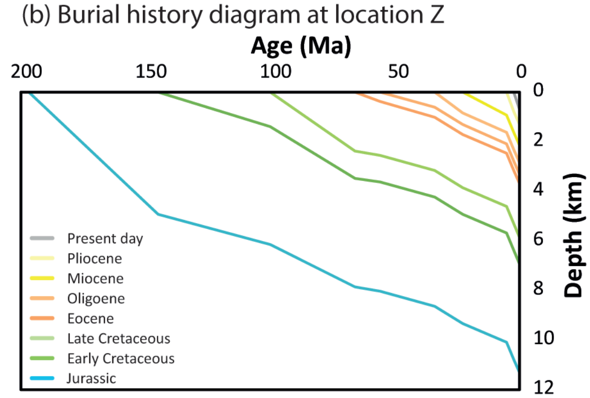

Figure 5

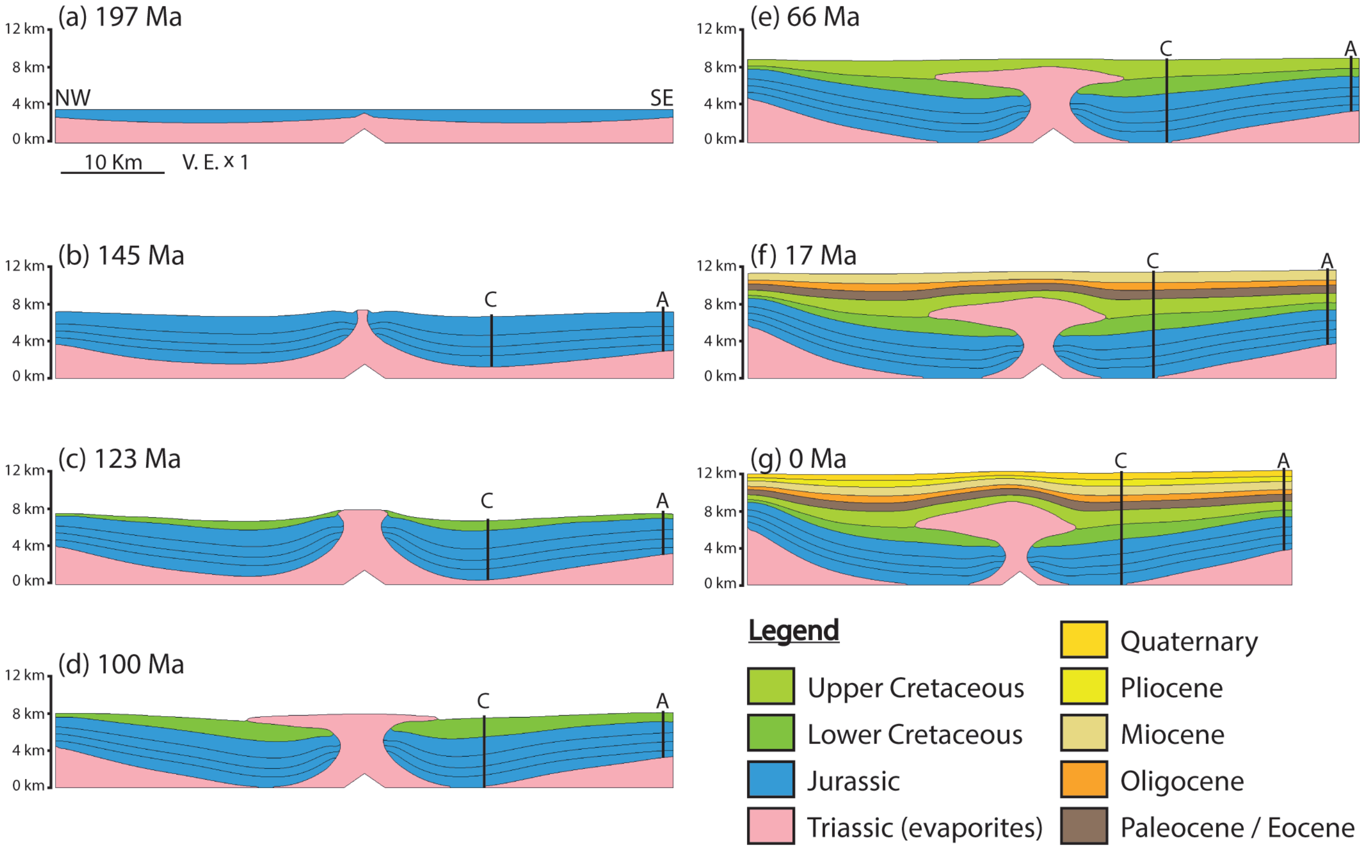

(a) 197 Ma
12 km
8 km
4 km
0 km
NW
SE
10 Km
V. E. x 1
(b) 145 Ma
C
A
(c) 123 Ma
(d) 100 Ma
(e) 66 Ma
(f) 17 Ma
(g) 0 Ma
Legend
Upper Cretaceous
Lower Cretaceous
Jurassic
Triassic (evaporites)
Quaternary
Pliocene
Miocene
Oligocene
Paleocene / Eocene

Figure 6

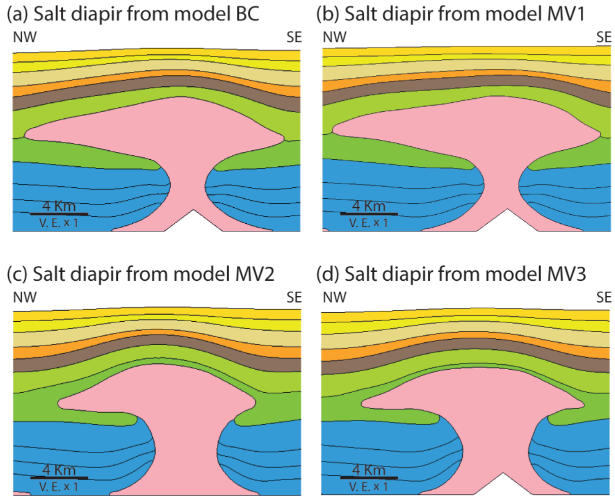
(a) Salt diapir from model BC
NW
SE
4 Km
V. E. x 1
(b) Salt diapir from model MV1
NW
SE
4 Km
V. E. x 1
(c) Salt diapir from model MV2
NW
SE
4 Km
V. E. x 1
(d) Salt diapir from model MV3
NW
SE
4 Km
V. E. x 1

Figure 7

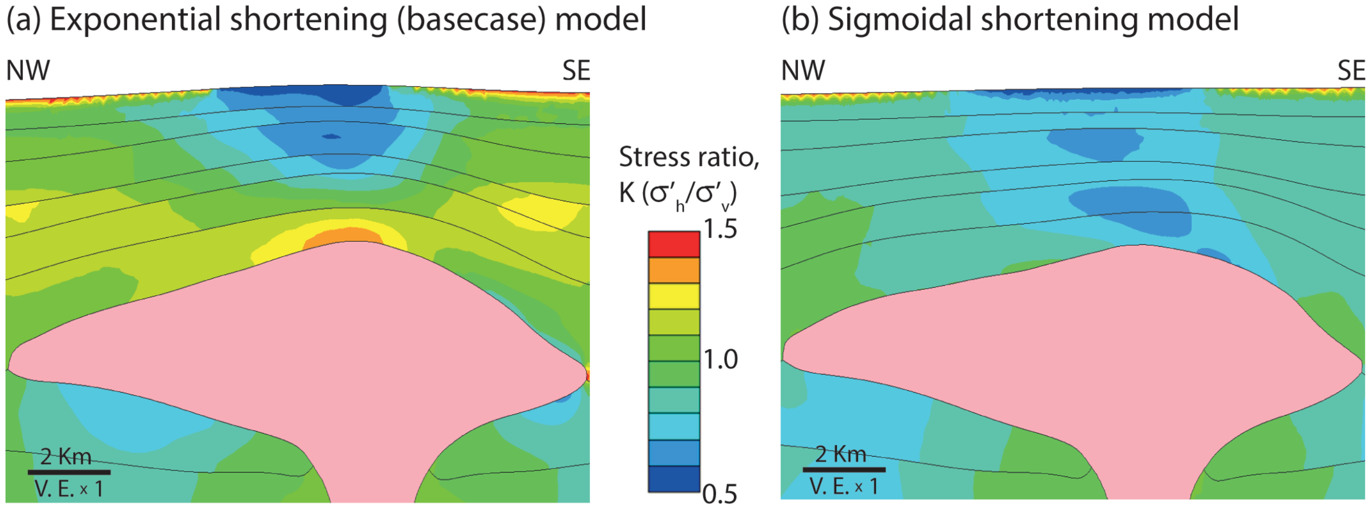
(a) Exponential shortening (basecase) model
(b) Sigmoidal shortening model
NW
SE
NW
SE
Stress ratio,
K (σ'_h/σ'_v)
1.5
1.0
0.5
2 Km
V. E. x 1
2 Km
V. E. x 1

Figure 8

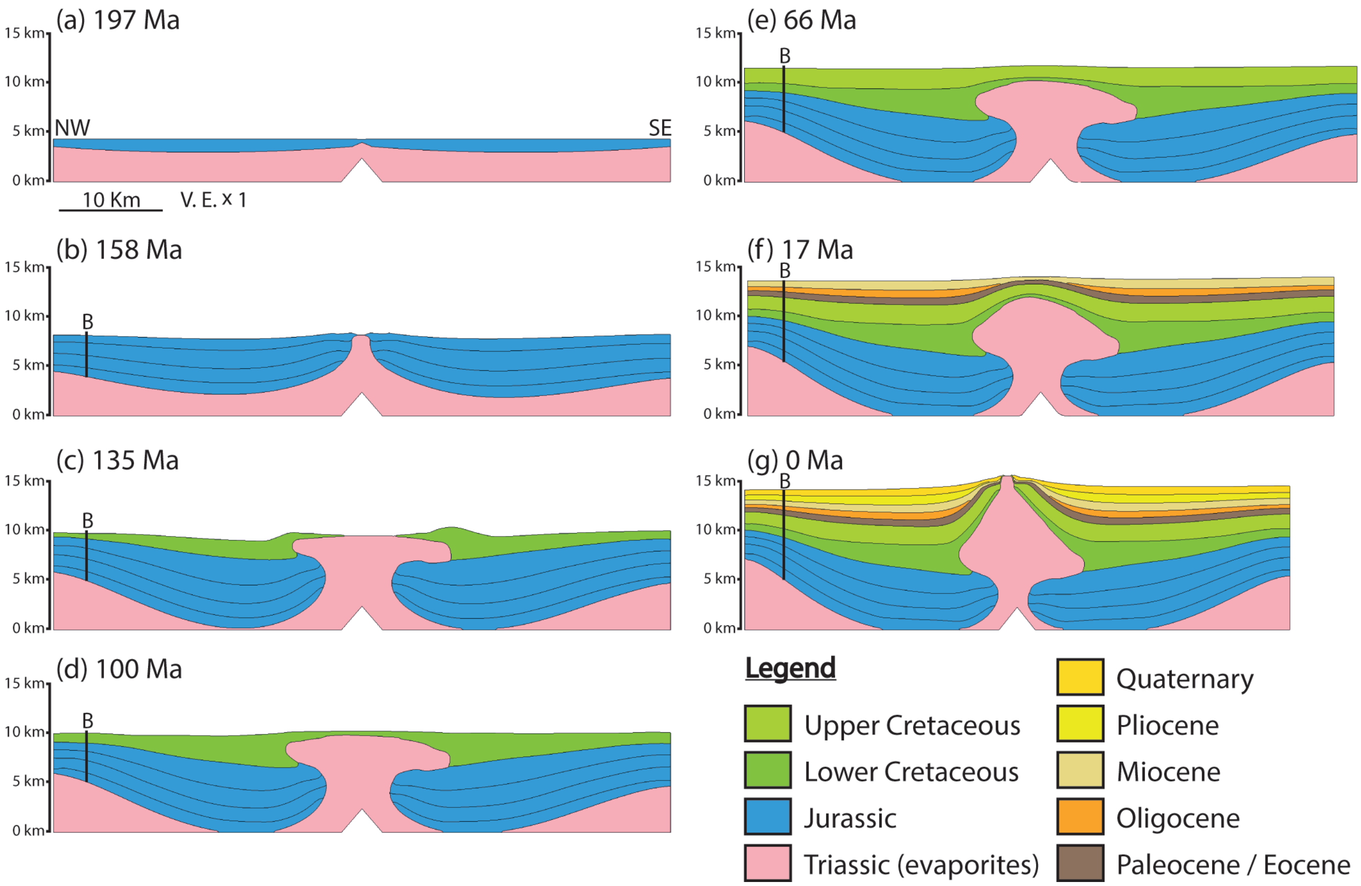

(a) 197 Ma
15 km
10 km
5 km
0 km
NW
SE
10 Km
V. E. x 1
(b) 158 Ma
B
(c) 135 Ma
(d) 100 Ma
(e) 66 Ma
(f) 17 Ma
(g) 0 Ma
Legend
Upper Cretaceous
Lower Cretaceous
Jurassic
Triassic (evaporites)
Quaternary
Pliocene
Miocene
Oligocene
Paleocene / Eocene

Figure 9

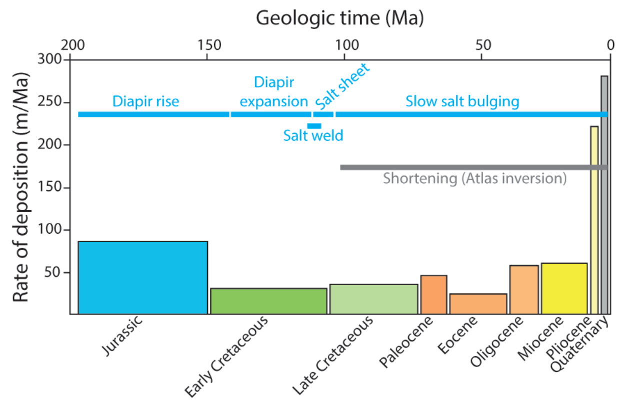

Geologic time (Ma)
200
150
100
50
0
300
250
200
150
100
50
Rate of deposition (m/Ma)
Diapir rise
Diapir expansion
Salt sheet
Slow salt bulging
Salt weld
Shortening (Atlas inversion)
Jurassic
Early Cretaceous
Late Cretaceous
Paleocene
Eocene
Oligocene
Miocene
Pliocene
Quaternary

Figure 10

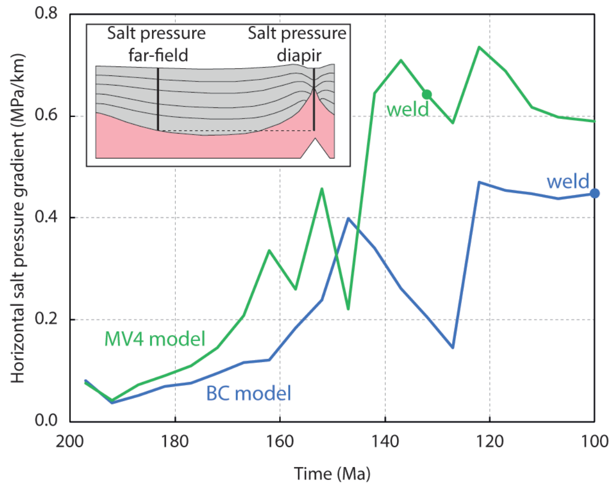
0.8
0.6
0.4
0.2
0.0
Horizontal salt pressure gradient (MPa/km)
Salt pressure
far-field
Salt pressure
diapir
weld
weld
MV4 model
BC model
200
180
160
140
120
100
Time (Ma)

Figure 11

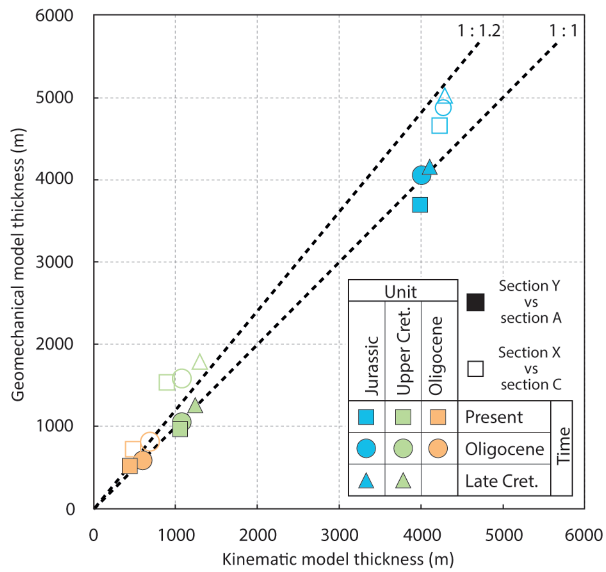

Geomechanical model thickness (m)
Kinematic model thickness (m)
0
1000
2000
3000
4000
5000
6000
1 : 1.2
1 : 1
Unit
Jurassic
Upper Cret.
Oligocene
Present
Oligocene
Late Cret.
Time
Section Y vs section A
Section X vs section C

Figure 12

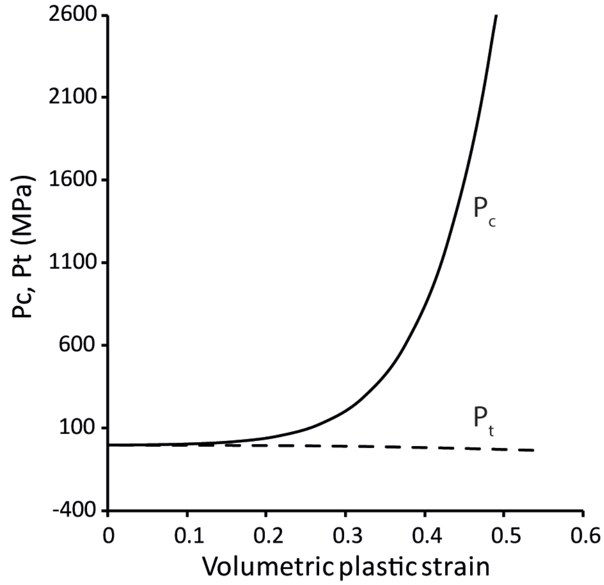

2600
2100
1600
1100
600
100
-400
Pc, Pt (MPa)
0
0.1
0.2
0.3
0.4
0.5
0.6
Volumetric plastic strain
P c
P t

Figure 13

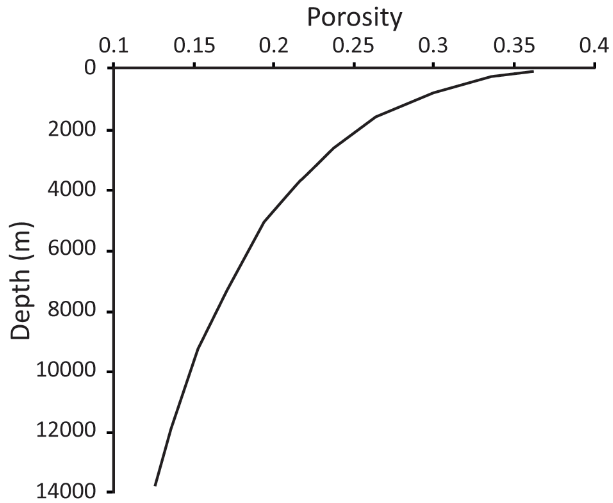
Porosity
0.1
0.15
0.2
0.25
0.3
0.35
0.4
0
2000
4000
6000
8000
10000
12000
14000
Depth (m)

Figure 14

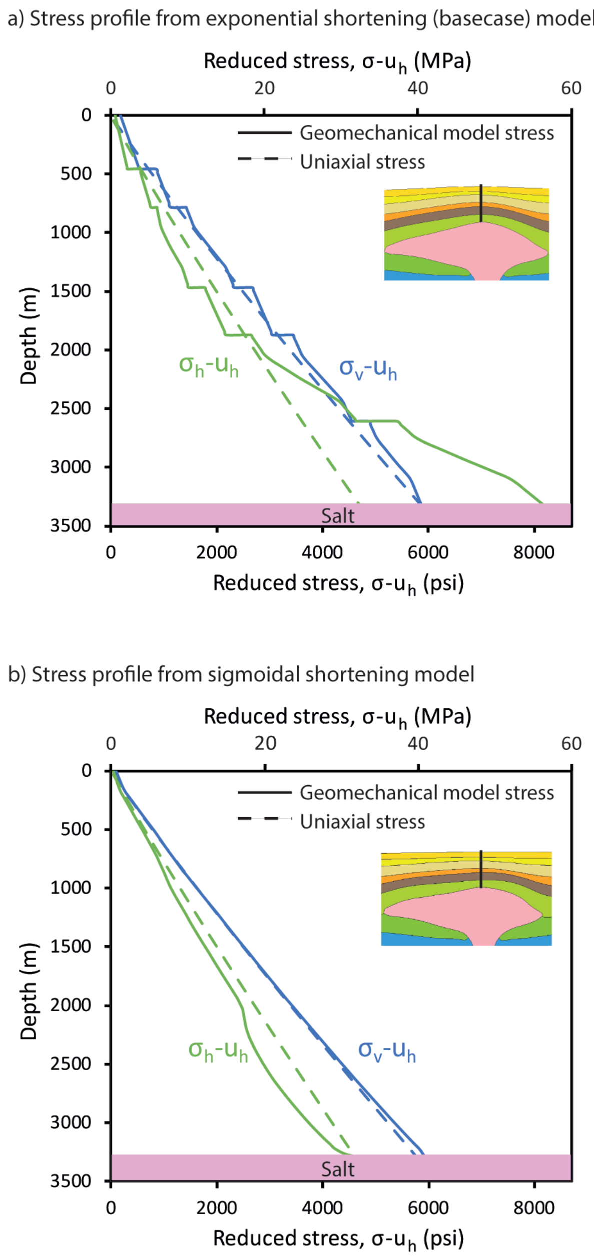
a) Stress profile from exponential shortening (basecase) model
Reduced stress, σ-u_h (MPa)
0
20
40
60
Depth (m)
0
500
1000
1500
2000
2500
3000
3500
Geomechanical model stress
Uniaxial stress
σ_h-u_h
σ_v-u_h
Salt
0
2000
4000
6000
8000
Reduced stress, σ-u_h (psi)
b) Stress profile from sigmoidal shortening model
Reduced stress, σ-u_h (MPa)
0
20
40
60
Depth (m)
0
500
1000
1500
2000
2500
3000
3500
Geomechanical model stress
Uniaxial stress
σ_h-u_h
σ_v-u_h
Salt
0
2000
4000
6000
8000
Reduced stress, σ-u_h (psi)

Figure 15